"Bismuth-Polyphenol Complex Incorporated Gquadruplex-Based Hydrogel for Efficient Visible Light Driven N₂ Fixation"

M.Sc. Thesis

by

SHAURYA



DEPARTMENT OF CHEMISTRY INDIAN INSTITUTE OF TECHNOLOGY INDORE May 2025

"Bismuth-Polyphenol Complex Incorporated Gquadruplex Based Hydrogel for Efficient Visible Light Driven N₂ Fixation"

A THESIS

Submitted in partial fulfillment of the requirements for the award of the degree

of

Master of Science

by

SHAURYA



DEPARTMENT OF CHEMISTRY INDIAN INSTITUTE OF TECHNOLOGY INDORE May 2025



INDIAN INSTITUTE OF TECHNOLOGY INDORE

DECLARATION

I hereby declare that the work which is being presented in the project entitled "Bismuth-Polyphenol Complex Incorporated G-quadruplex Based Hydrogel for Efficient Visible Light Driven N₂ Fixation." is the partial fulfillment of the requirements for the award of the Degree of Masters of Science and submitted to the Department of Chemistry, Indian Institute of Technology Indore, is an authentic record of my work carried out during the period from July, 2024 to May, 2025 under the supervision of **Dr. Tridib Kumar Sarma**, Associate professor, Department of Chemistry, IIT Indore.

I have not submitted the matter presented in this thesis for the award of any other degree of this or any other institute.

21 05 2025

Signature of the student with date (Shaurya)

This is to certify that the above statement made by the candidate is accurate, complete, and correct to the best of my knowledge and belief.

Tricile X Suma

Signature of the supervisor with date
(Dr. Tridib Kumar Sarma)

ACKNOWLEDGEMENTS

I would like to express my sincere gratitude to my project supervisor, Dr.

Tridib Kumar Sarma, for allowing me to conduct research within his

esteemed group. His expert guidance, thoughtful advice, and constant

encouragement helped me throughout my project work.

My heartfelt thanks go to the Department of Chemistry faculty members for

their constructive feedback and continuous support. The department's

resources and facilities played an essential role in my research. I would also

like to extend my appreciation to SIC, IIT Indore, and its team for their

technical support and assistance throughout my research. For XPS, I am

grateful to SAPTRISHI at IIT Jammu and for ESR and TEM facilities, to

SAIF at IIT Bombay for their essential support and collaboration.

I would like to give special recognition to Mr. Tarun Kumar Sahu, my

mentor, whose ongoing guidance and valuable insights have been crucial

throughout this project. My sincere gratitude is also extended to my lab

mates, namely Ms. Amrita, Ms. Vidhi, Mr. Surya Kamal, Mr. Aditya, and

Mr. Ravindra, for their assistance in both academic and non-academic

matters. I am deeply grateful to all my friends and batchmates.

Finally, I would like to convey my deepest gratitude to my family for their

unwavering support.

Shaurya

2303131024

VII

Dedicated to my grandfather....



ABSTRACT

The utilization of natural renewable resources for the development of functional material offers significant economic and environmental advantages. Polyphenols, particularly caffeic acid (CA), direct the selfassembly of biomacromolecules through non-covalent interactions. In this study, a unique strategy was employed to design sustainable functional materials through polyphenol-directed assembly of nucleotides, addressing challenges associated with long-chain oligonucleotides. Using caffeic acid, a less-explored plant-derived polyphenol, guanosine 5'-monophosphate (GMP) was self-assembled into catechol-functionalized G-quadruplex well-defined helical fibrils with tunable hydrogels, forming physicochemical properties. These hydrogels enabled the precise spatial confinement of metal-polyphenol complexes, offering nanoscale control over material properties. Bismuth, chosen for its visible-light absorption, tunable band gaps, and environmental compatibility, was incorporated to exploit its photocatalytic potential. The GC-Bi hydrogel demonstrated exceptional nitrogen fixation performance, achieving an ammonia yield of 905.2 µmol h⁻¹ g⁻¹ (cat.), nearly 3.8 times higher than the pristine CBi complex, with superior selectivity for NH₃. Structural, morphological, and spectroscopic analyses revealed the in-situ heterojunction formation, which results in enhanced charge separation and suppressed electron-hole recombination, underscoring the transformative potential of supramolecular design for scalable applications in environmental remediation, energy conversion, and carbon capture.

TABLE OF CONTENTS

LIST OF FIGURES
NOMENCLATURE
ACRONYMS
Chapter 1
1.1 Introduction1-4
Chapter 2
2.1 Literature Survey5-8
Chapter 3
3.1 Motivation9-10
3.2 Objective
Chapter 4
4.1 Experimental Section
Chapter 5
5.1 Results and Discussion
Chapter 6
6.1 Conclusion
6.2 Future Scope58
Chapter 7
7.1 References
7.2 Supporting Figures 63-69

LIST OF FIGURES

- **Figure 1.** Structures of the most common natural polyphenols.
- Figure 2. Multiple interactions of polyphenols include (a) covalent cross-linking, (b) hydrogen-bonding, (c) hydrophobic interaction, (d) coordination interaction, (e) electrostatic interaction, and (f) π - π stacking.
- **Figure 3.** Several metal-phenolic interactions.
- **Figure 4.** Metal-polyphenol networks with their properties and potential applications.
- Figure 5. (a) The interfacial assembly process on different substrates, (b) Different interactions between proteins and polyphenols exemplified for the representative amino acids Lys (lysine), Ser (serine), and Phe (phenylalanine), (c) Coating of sacrificial template and subsequent capsule formation, and (d) Examples of biotechnological applications of protein–polyphenol capsules.
- **Figure 6.** (a) Schematic representation of the assembly of DNA-TA particles: (I) loading of CaCO₃ particles with DNA (yDNA or plasmid DNA), (II) cross-linking by TA, and (III) removal of CaCO₃ template core to yield DNA-TA particles with the possible interactions involved in the stabilization of the DNA-TA assemblies.
- **Figure 7.** Schematic representation of the Supramolecular Assembly of TA and ssDNA.
- **Figure 8.** Structure of four principal nucleotides of DNA.
- **Figure 9.** GMP and their most common self-assembled structures.
- **Figure 10.** (a) UV-Vis absorption curves of Nessler's reagent assays with various concentrations of NH₄⁺, and (b) A calibration curve for estimating the concentrations of NH₄⁺. (Inset:

- digital photograph of concentration-dependent complex formation of NH₄⁺ with Nessler's reagent).
- Figure 11. (a) UV-Vis spectra obtained using standard solutions of NH₄Cl after reaction with indophenol blue, and (b) and the resulting linear calibration curve. (Inset: digital photograph of concentration-dependent complex formation of NH₄⁺ with indophenol blue).
- Figure 12. (a) UV-Vis spectra of standard N₂H₄ solutions after reaction with a colorimetric reagent, and (b) the resulting linear calibration curve. (Inset: digital photograph of concentration-dependent complex formation of N₂H₄).
- Figure 13. (a) Formation of the GMP-CA hydrogel along with its thermoreversible nature, (b) FESEM image, (c) TEM image, and (d) AFM image of the GC hydrogel (inset: height profile of the fiber morphology).
- **Figure 14.** (a) UV-visible spectra of GMP, CA and GC hydrogel, (b) FTIR of GMP, CA and GC xerogel, (c) Zeta potential analysis for GC, GBi and GC-Bi, (d) ³¹P NMR, (e) ¹H NMR of GMP and GC hydrogel, and (f) CD spectra of GMP, CA and GMP-CA hydrogel.
- Figure 15. (a) Fluorescence spectra of ThT, GBi + ThT and GC+ThT, (b) PXRD pattern of GC, GBi, GC-Bi and CBi and (c) Plausible structures of G-quartet formation governed by CA.
- **Figure 16.** Gelation mechanism of GC hydrogel induced via G-quadruplex formation.
- **Figure 17.** Zeta potential analysis for GC, GBi and GC-Bi hydrogels
- **Figure 18.** Photographic image of metal ion-induced coordination cross-linking in catechol-functionalized G-quadruplex GC hydrogels.

- **Figure 19.** (a) Varying the conc. (mM) of Bi³⁺ keeping the conc. of GMP (125 mM) and CA (100 mM) constant, (b) GBi hydrogel at 125:40 mM conc. respectively.
- Figure 20. (a) Formation of the GC-Bi hydrogel along with its thermoreversible nature, (b) FESEM image, (c) TEM, and (d) AFM images of the GC-Bi hydrogel, (e) Formation of the GBi hydrogel along with its thermoreversible nature, (f) FESEM, (c) TEM, and (d) AFM images of the GBi hydrogel.
- **Figure 21.** (a) Synthetic scheme, (b) FESEM image, (c) EDX elemental mapping of C, Bi, and O, and (d) FT-IR spectra of CBi complex.
- **Figure 22.** (a) UV-Vis absorption spectra of prepared samples with respect to GMP, (b, c) FTIR spectra of GC-Bi with respect to their components, (d) PXRD pattern of prepared samples, (e) FT-IR spectra of GMP and GBi, (f) and CD spectra of prepared samples with respect to GMP.
- Figure 23. Plausible structures of G-quartet formation governed by (a)

 Bi³⁺ and (b) cross-linking of G-quartets obtained by GC and GBi.
- Figure 24. (a) Photographic images of powdered GBi, CBi and GC-Bi, (b) UV-Vis spectra, (c) and Band Gap Calculations using Tauc's Plot of GBi, CBi and GC-Bi.
- Figure 25. (a) The NH₄ ⁺ yield using prepared catalysts under white light irradiation in N₂, (b) Effect of bismuth ion concentration (10–50 mM) on NH₄ ⁺ yield for GC-Bi catalysts, (c) Nitrogen fixation performance through controlled experiments, (d)The NH₄ ⁺ production rates using GC-Bi as a photocatalyst, (e) selective production of NH₃, (f) ¹H NMR of standard NH₃ and produced NH₃.

- **Figure 26.** (a) N₂ Adsorption-desorption curves of CBi, GBi and GC-Bi, (b) Comparison of pore size, specific surface area, and pore volume for CBi, GBi, and GC-Bi catalysts.
- **Figure 27.** (a) Bi 4f, (b) P 2p, (c) and O 1s XPS spectra of CBi, GBi, and GC-Bi, (d) EPR spectra, (e) and Fluorescence spectra of CBi, GBi, and GC-Bi.
- **Figure 28.** (a) Tauc's plot, (b) VB-XPS spectra, (c) Energy band gap structure of GC-Bi containing both CBi and GBi.
- **Figure 29.** Plausible mechanism for photocatalytic nitrogen reduction reaction (PNRR).
- Figure 30. (a) Dynamic strain sweep of the GC, GBi, and GC-Bi gels conducted at a constant angular frequency of 10 rad/s, (b) frequency sweep tests of the GC, GBi, and GC-Bi metalogels at a constant strain of 1%, (c) thixotropic loop analysis for the GC, (d) GBi, and (e) GC-Bi metalogel.
- **Figure S1.** Comparison of ThT fluorescence increase in the previously reported G-assemblies systems with GBi and GC.
- **Figure S2.** UV-Vis absorbance spectra of GC-Bi gel with varying Bi³⁺ conc. (10–50 mM).
- **Figure S3.** Concentration-dependent rheological experiment on GC-Bi hydrogels by varying Bi³⁺ conc. from 10 mM to 80 mM.
- **Figure S4.** EDX (C, N, O, P, Na, Bi) of GBi gel.
- **Figure S5.** EDX (C, N, O, P, Na, Bi) of GC-Bi gel.
- **Figure S6.** CD spectra of GBi gel with varying Bi³⁺ conc. (0–50 mM).
- **Figure S8.** (a) Bi 4f XPS spectra, (b) SEM image, (c) and PXRD spectra of recycled GC-Bi.
- **Figure S9.** Thermogravimetric analysis of CBi, GBi, and GC-Bi.
- **FigureS10.** Pore size and pore volume analysis of CBi, GBi, and GC-Bi.
- **Figure S11.** XPS survey spectra of CBi, GBi, and GC-Bi.

NOMENCLATURE

mg Milligram

g Gram

 μL Microliter

mL Milliliter

mM Millimolar

μM Micromolar

min Minute

M Molar

% Percentage

rpm Rotation per minute

rt Room temperature

s Seconds

 $^{\circ}C$ Degree Celsius

h Hour

nm Nanometer

rad/s Radian per second

ACRONYMS

MOFs Metal Organic Frameworks

CPs Coordination Polymers

CPNDs Coordination Polymer Nanodots

TA Tannic acid

EA Ellagic acid

GA Gallic acid

CA Caffeic acid

GMP Guanosine Monophosphate

ThT Thioflavin T

 Λ_{ex} Excitation wavelength

 Λ_{em} Emission wavelength

BE Binding Energy

UV-Vis Ultraviolet-Visible

FTIR Fourier Transform Infrared

CD Circular Dichroism

XPS X-ray Photoelectron Spectroscopy

Brunauer-Emmet Isotherm

PXRD Powder X-ray Diffraction

TGA Thermogravimetric Analysis

EDX Energy Dispersive X-ray

Spectroscopy

FESEM Field emission scanning electron

microscope

TEM Transmission electron microscope

AFM Atomic force microscopy

EPR Electron proton resonance

CHAPTER 1

1.1 INTRODUCTION

Polyphenols, a major group of phytochemicals, have drawn significant attention due to their several biological properties, such as antioxidant, anti-inflammation, anticancer, antimicrobial, antiviral, and anti-obesity properties. Owing to their excellent biological properties, polyphenol-based materials have applications as antibiotics, antidiarrheal, anti-ulcer, and anti-inflammatory agents, and therefore, polyphenols are essential parts of human and animal diets. The most common polyphenols include tannic acid (TA), gallic acid (GA), ellagic acid (EA), caffeic acid (CA), curcumin, and epigallocatechin gallate (EGCG)³ (Figure 1).

Figure 1. Structures of the most common natural polyphenols.

In addition to their remarkable biological properties, polyphenols exhibit diverse physical and chemical characteristics owing to the abundance of hydroxyl groups and aromatic rings in their structure. They exhibit diverse interactions that enable their assembly into complex supramolecular structures, including covalent cross-linking through oxidative polymerization, which imparts stability and strength; hydrogen bonding via their hydroxyl groups, facilitating reversible and dynamic networks; and

hydrophobic interactions from their aromatic cores, promoting aggregation in aqueous systems.⁴ Additionally, they form coordination complexes with metal ions through catechol and gallol groups, enabling pH-responsive and stimuli-adaptive assemblies. Electrostatic interactions arise from their ionizable phenolic groups, enhancing binding with charged biomolecules, while π - π stacking between their planar aromatic rings reinforces structural order (Figure 2). These synergistic interactions make polyphenols versatile building blocks for designing multifunctional materials ⁵

a)
$$R \longrightarrow OH \qquad HO \longrightarrow OH \qquad OH$$

$$R \longrightarrow OH \qquad HO \longrightarrow OH \qquad HO \longrightarrow OH$$

$$R \longrightarrow OH \qquad HO \longrightarrow OH \qquad HO \longrightarrow OH$$

$$R \longrightarrow OH \qquad HO \longrightarrow OH \qquad HO \longrightarrow OH$$

$$R \longrightarrow OH \qquad HO \longrightarrow OH \qquad HO \longrightarrow OH$$

$$R \longrightarrow OH \qquad HO \longrightarrow OH \qquad HO \longrightarrow OH$$

$$R \longrightarrow OH \qquad HO \longrightarrow OH \qquad HO \longrightarrow OH$$

$$R \longrightarrow OH \qquad HO \longrightarrow OH \qquad HO \longrightarrow OH$$

$$R \longrightarrow OH \qquad HO \longrightarrow OH \qquad HO \longrightarrow OH$$

Figure 2. Multiple interactions of polyphenols include (a) covalent crosslinking, (b) hydrogen-bonding, (c) hydrophobic interaction, (d) coordination interaction, (e) electrostatic interaction, and (f) π - π stacking.

Based on these interactions, they exhibit a remarkable ability to interact with biomolecules, enabling the formation of high-order supramolecular structures with tunable properties. Their interaction with proteins facilitates the development of functional hydrogels and nanocapsules, such as tannic acid-protein assemblies used in catalysis and biomedical applications. Polyphenols also stabilize nucleic acids, promoting the formation of G-quadruplex architectures, exemplified by guanosine monophosphate hydrogels, which exhibit unique optical and electronic properties. Additionally, polyphenols enhance the structural integrity of

oligonucleotides, forming ordered frameworks utilized in gene delivery systems and siRNA-based therapies by protecting genetic material from degradation and enabling effective cellular uptake. These interactions underscore their applications ranging from gene delivery systems to functional biomaterials with tailored permeability and mechanical properties. Polyphenols, with their catechol and gallol groups, can interact with metals and play a pivotal role in the functional diversification of polyphenol-based materials. Acting as natural ligands, polyphenols coordinate with metal ions to form metal-polyphenol networks (MPNs), where electron-rich polyphenols donate nonbonding electrons to the vacant orbitals of metals. These interactions vary depending on the type of metal ion: alkali and alkaline earth metals interact via cation- π interactions, transition metals through coordination bonding, noble metals via redox interactions, and metalloids through dynamic covalent bonding. The pH of the phenolic solution and the electronic configuration of the metal ions critically influence MPN formation, dictating the type and color of complexes formed, with multivalent transition metals producing vibrant networks due to d-d transitions⁶ (Figure 3).

Figure 3. Several metal-phenolic interactions.

These unique features have been harnessed in designing multifunctional biomaterials with tunable properties for applications in the fields of cell biology, cancer theranostics, drug delivery, metabolic syndrome treatment, magnetic resonance imaging, photothermal therapy, sodium-ion batteries, catalysis, high-performance supercapacitors, etc⁷ (Figure 4).

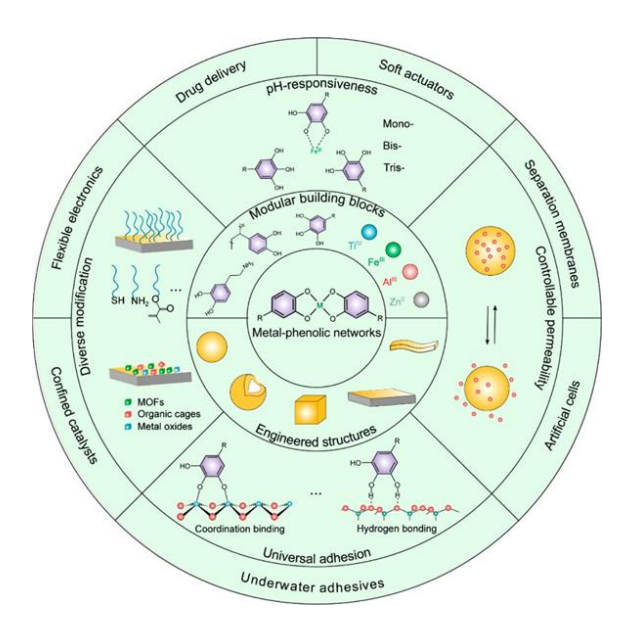


Figure 4. Metal-polyphenol networks with their properties and potential applications.⁷

CHAPTER 2

2.1 LITERATURE SURVEY

In 2020, Frank Caruso and his research group developed a versatile, onepot interfacial assembly method for constructing functional proteinpolyphenol films and capsules using tannic acid (TA) and diverse proteins⁸ (Figure 5). This water-based strategy, performed under ambient conditions, capitalizes on the rich multivalent chemistry of TA, which forms noncovalent networks with proteins via hydrogen bonding, hydrophobic, and ionic interactions. The method enables rapid and uniform coating across a variety of substrates, planar, spherical, and biological, without the need for chemical modification or complex instrumentation. By depositing protein-TA complexes onto sacrificial templates such as silica and subsequently removing them, stable and biocompatible hollow capsules can be formed. These assemblies preserve the native bioactivity of proteins and exhibit tunable responsiveness to pH and ionic environments. Compared to traditional protein immobilization techniques, this approach provides superior conformity, dynamic functionality, and structural integrity, with demonstrated applications in enzymatic catalysis, targeted delivery, and multifunctional biointerfaces.

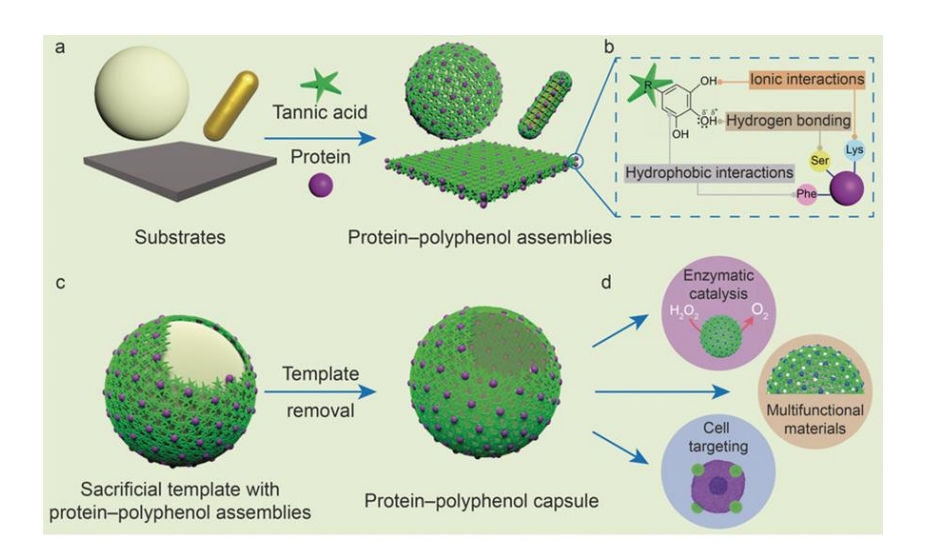


Figure 5. (a) The interfacial assembly process on different substrates, (b) Different interactions between proteins and polyphenols exemplified for the representative amino acids Lys (lysine), Ser (serine), and Phe (phenylalanine), (c) Coating of sacrificial template and subsequent capsule formation, and (d) Examples of biotechnological applications of protein–polyphenol capsules.⁸

Ou et al. (2023) developed a supramolecular co-assembly approach for fabricating DNA-polyphenol microparticles by leveraging the multivalent interactions between tannic acid (TA) and nucleic acids⁹ (Figure 6). Using a simple, template-assisted assembly process where DNA (including Yshaped, plasmid, ssDNA, or dsDNA) was adsorbed onto porous CaCO₃ microparticles, followed by TA-mediated cross-linking. The resulting coreshell structures were treated with EDTA, which chelates calcium ions to dissolve the CaCO₃ core, yielding hollow DNA-TA particles with tunable morphology, including toroids and capsules. The assembly was stabilized through hydrogen bonding and π - π stacking, forming compact nanostructures that exhibited remarkable serum stability and resistance to nuclease degradation. These particles enabled co-delivery of immunostimulatory CpG motifs and model antigens (OVA). This work

expands the application of polyphenol-mediated assemblies from proteins to nucleic acids, establishing a scalable, biodegradable, and immunoactive system for gene and vaccine delivery.

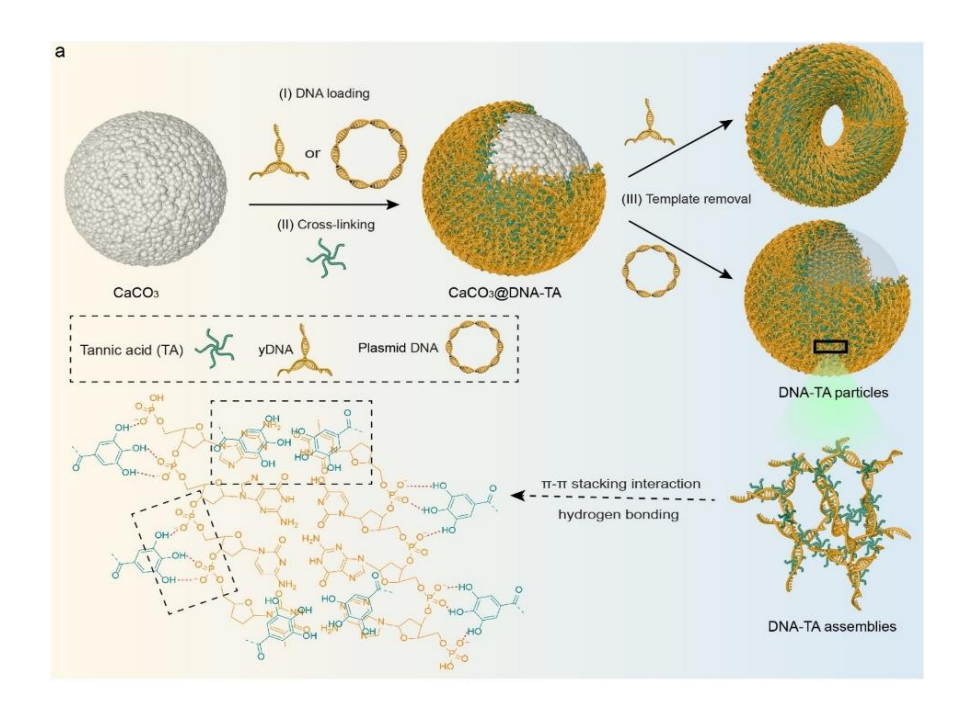


Figure 6. (a) Schematic representation of the assembly of DNA-TA particles: (I) loading of CaCO₃ particles with DNA (yDNA or plasmid DNA), (II) cross-linking by TA, and (III) removal of CaCO₃ template core to yield DNA-TA particles with the possible interactions involved in the stabilization of the DNA-TA assemblies.⁹

In 2023, a simple, template-free strategy was introduced by Frank Caruso, Francesca Cavalieri and their co-workers for synthesizing uniform oligonucleotide–polyphenol nanoparticles (TA–ODN NPs) by exploiting the thermal disaggregation and reassembly of tannic acid (TA) with single-stranded oligonucleotides (Figure 7). At room temperature, mixing aggregated TA with ODNs led to the formation of polydisperse particles (100 nm–2 μ m). However, controlled thermal cycling on heating to 90 °C followed by gradual cooling to 25 °C—induced the disassembly of TA

clusters and enabled the precise supramolecular organization of TA and ODNs into stable, monodisperse nanoparticles ($\sim 100\,\mathrm{nm}$). These assemblies were stabilized through hydrogen bonding and $\pi - \pi$ stacking interactions, avoiding the need for metal ions or synthetic polymers. The resulting TA–ODN NPs exhibited excellent colloidal stability, high DNA loading efficiency, and serum resistance. When loaded with immunostimulatory CpG motifs, they showed efficient macrophage uptake, lysosomal trafficking, and a 7-fold increase in TNF- α secretion compared to free CpG, confirming their potential as non-toxic, immunoactive platforms for intracellular nucleic acid delivery and vaccine development.

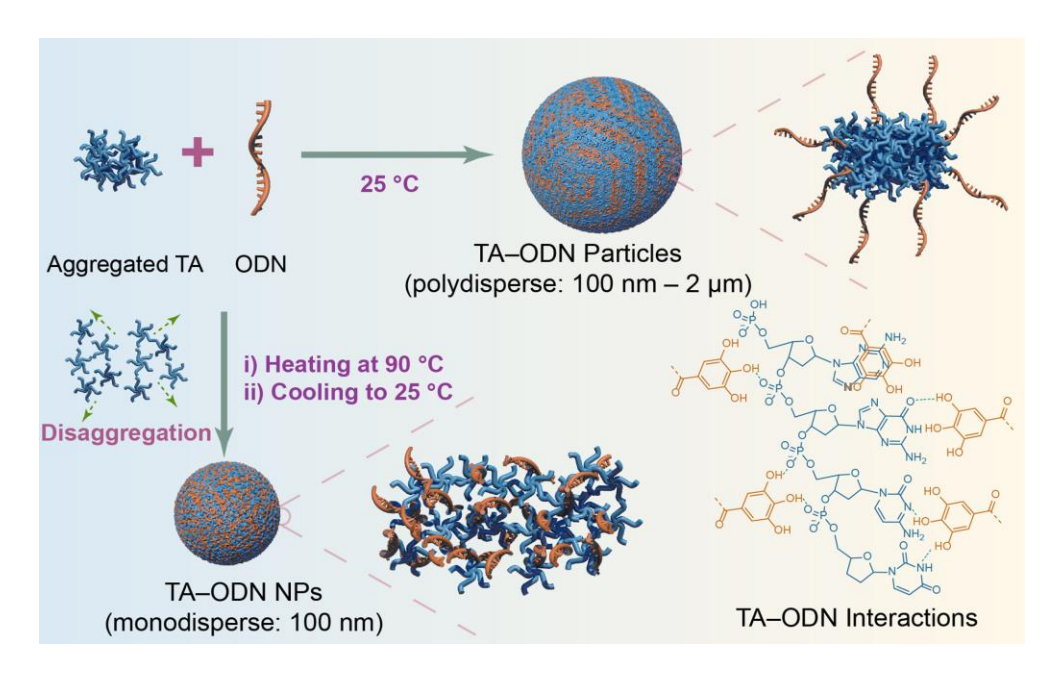


Figure 7. Schematic representation of the Supramolecular Assembly of TA and ssDNA.¹⁰

CHAPTER 3

3.1 MOTIVATION

Nucleotides, regarded as the essential constituents of nucleic acids, are composed of a nitrogenous base, a phosphate group, and a sugar moiety. Among the four principal nucleotides- adenosine monophosphate (AMP), thymidine monophosphate (TMP), cytidine monophosphate (CMP), and guanosine monophosphate (GMP), variations in their base structure have been recognized to impart distinct self-assembly and structural characteristics¹¹ (Figure 8). In most cases, supramolecular DNA-based materials have been constructed using oligonucleotide strands with defined sequences and predictable secondary structures. Although such systems allow for precise control over assembly, their preparation often involves high synthesis costs, structural fragility, and increased design complexity, limiting their broader applicability in adaptive material systems.

Figure 8. Structure of four principal nucleotides of DNA.

In response to these limitations, a simplified strategy was considered, in which a single nucleotide unit was employed as a minimal scaffold capable of engaging in directed self-assembly with polyphenols. Instead of utilizing long-chain oligonucleotides, a monomeric nucleotide was examined for its capacity to generate ordered supramolecular assemblies under mild conditions. Among the canonical nucleotide units, GMP was identified as a

promising candidate, owing to its well-documented tendency to undergo spontaneous self-organization into defined supramolecular structures. Compared to other nucleotides, GMP has been shown to form more stable and diverse supramolecular structures. This behavior has been attributed to the purine ring, which enables extensive π – π stacking interactions along with multiple hydrogen-bonding sites. In contrast, pyrimidine-based nucleotides such as TMP and CMP possess fewer interaction points and exhibit limited self-association. As a result, GMP has been widely investigated for its capacity to organize into highly ordered architectures, including G-ribbons, G-dimers, and G-quartets^{12,13} (Figure 9). These assemblies have been recognized for their intrinsic stability and structural versatility in both solution and solid-state environments.

Figure 9. GMP and their most common self-assembled structures.

In this study, GMP has been viewed as the core structural unit for coassembly with polyphenolic compounds. The hydroxyl-rich, aromatic framework of polyphenol allows for cooperative hydrogen bonding and aromatic interactions with GMP, forming hybrid networks without the need for covalent modification or external templates. Through the utilization of GMP as a minimal, naturally occurring self-assembling unit, the potential to construct structurally tunable and compositionally simple hybrid materials has been explored. By coupling GMP with polyphenols, a new class of nucleotide-polyphenol materials has been investigated, with an emphasis on non-covalent assembly, environmental responsiveness, and functional tunability.

3.2 OBJECTIVE

This work aims to construct hierarchically ordered supramolecular structures through the self-assembly of guanosine monophosphate (GMP) in the presence of a less-explored polyphenol, caffeic acid (CA). Caffeic acid, with its catechol and carboxylic functionalities, offers multiple hydrogen bonding sites, π - π stacking ability, and metal-coordination potential, making it a suitable candidate for guiding GMP assembly under aqueous conditions. A simple and template-free synthetic approach will be employed to facilitate the polyphenol-directed self-assembly of GMP into higher-order architectures. The nature and role of non-covalent interactions involved in the assembly process will be systematically investigated using spectroscopic and morphological techniques. To further enhance the functional scope of the system, different metal ions will be incorporated into the GMP-CA framework to tune the structural features, functionality, stability, and responsiveness. Using this framework, the study aims to develop a sustainable and versatile platform, enabling the exploration of previously unexplored applications in soft material design, biointerfaces, and stimuli-responsive systems.

CHAPTER 4

4.1 EXPERIMENTAL SECTION

This report primarily focuses on the polyphenol-directed assembly of guanosine monophosphate (GMP) and the confinement of a bismuth–polyphenol complex within a hydrogel matrix, aiming toward potential applications in visible-light-driven photocatalysis. The hydrogel system is constructed using the disodium salt of GMP as a low molecular weight supramolecular gelator, caffeic acid (CA) as a naturally derived polyphenolic crosslinker, and bismuth nitrate pentahydrate as the source of Bi³⁺ ions. This strategy enables the in-situ formation of a hybrid network that integrates organic and inorganic components, offering structural versatility and enhanced photocatalytic properties under visible light irradiation.

4.1.1 Materials:

All chemicals used in the experiments are of analytical grade and were used as received without further purification. All experiments were conducted at ambient conditions. The following chemicals were purchased from SRL, India: Guanosine monophosphate disodium salt (GMP), Thioflavin T (ThT), hydrazine hydrate (N₂H₄.H₂O), ammonium chloride (NH₄Cl), sodium hypochlorite (NaOCl), sodium nitroprusside (Na₂[Fe(CN)₅NO]) and to prepare the chromogenic reagent (salicylic acid, sodium potassium tartrate, sodium hydroxide (NaOH)) for indophenol blue method test, sulfamic acid, Greiss's reagent for NO₂⁻ detection. Caffeic acid from BLD Pharmatech (India) Pvt. Ltd, bismuth nitrate pentahydrate from Sigma Aldrich, Nessler's reagent from Loba Chemie Pvt. Ltd. Deuterium oxide (D₂O) and deuterated dimethyl sulfoxide (DMSO-d6) for NMR analysis was obtained from TCI. HPLC water from SRL, India, was used throughout the experiments. To prepare the colouring agent for hydrazine test, *p*-

dimethylaminobenzaldehyde from SRL, HCL from Advent and ethanol was obtained from Merck.

4.1.2 Instrumentation and Methods:

4.1.2.1 Rheological Measurements

Rheological analysis was conducted using an Anton Paar Physica MCR 301 rheometer equipped with a 25 mm parallel plate geometry. Dynamic strain sweep tests were performed at a fixed angular frequency (ω) of 10 rad/s, while frequency sweep experiments were carried out at a constant strain (γ) of 1% at 25 °C. Thixotropic step-strain measurements were executed by applying alternating strain levels of 1% and 500% at a constant angular frequency of 10 rad/s, with measurements taken over specific time intervals.

4.1.2.2 Fourier-transformed Infrared (FTIR) spectroscopy and PXRD Measurements

FTIR analysis was performed using a Bruker Alpha II spectrometer, operating in the range of 400–4000 cm⁻¹ with a resolution of 4 cm⁻¹. Powder X-ray diffraction (PXRD) measurements were conducted with a Rigaku SmartLab instrument utilizing a Cu Kα source, producing X-rays with a wavelength of 0.154 nm. Hydrogels are lyophilized and powdered xerogel were used for both FTIR and PXRD measurements.

4.1.2.3 UV-Visible and Circular Dichroism (CD) Spectroscopy

UV-Vis spectra were recorded using an Agilent Cary 60 UV-Vis Spectrometer, while circular dichroism (CD) spectra were obtained with a JASCO J-815 Spectropolarimeter. Both sets of measurements were carried out in a quartz cell with a 1 mm path length, with the UV-absorption spectra spanning the range of 220–800 nm and the CD spectra measured between 200–400 nm.

4.1.2.4 Steady-state Fluorescence Measurements

Steady-state fluorescence (FL) spectra were acquired using a Fluoromax-4p spectrofluorometer (model: FM-100) from Horiba JobinYvon. All the FL experiments using ThT were performed in the same approach with a constant concentration of $10~\mu\text{M}$, using a $10x10~\text{mm}^2$ cuvette. However, the steady-state fluorescence spectra of the prepared catalysts were recorded using water as the solvent.

4.1.2.5 Zeta Potential Measurements

Zeta potential measurements were performed using a Nanoplus Zeta Potential Analyzer, using a quartz flow cell, and the samples were measured after 100-fold dilution.

4.1.2.6 Surface Area Analysis and Thermal Stability

For the Brunauer-Emmett-Teller (BET) surface area analysis, Autosorb iQ2 by Anton Paar Quantachrome instrument was used. Thermal stability was determined by Mettler Toledo TGA/DSC 1 thermogravimetric analyzer.

4.1.2.7 XPS spectroscopic Measurements

X-ray photoelectron spectroscopy (XPS) analysis was studied with the help of Thermoscientific NEXSA Surface analyzer.

4.1.2.8 EPR spectroscopic Measurements

EPR spectra were recorded using JEOL (Japan), JES_FA 200 ESR spectrometer with X band at room temperature.

4.1.2.9 Microscopic characterizations

Field emission scanning electron microscopy (FESEM) images were taken on Carl Zeiss Supra 55 instruments. The samples were diluted up to 200 times in HPLC water, and 10 μ l of it was drop-casted on a clean piece of glass slide and left to air dry for 24 hours. The drop-casted sample was then coated with Au and imaged under the SEM. A Bruker EDX (Energy

Dispersive X-ray) instrument was used for EDX analysis. Transmission Electron microscope (TEM) images were taken from the electron microscope of model JEM-2100 at an accelerating voltage of 200 kV. 5 µl of the same samples were drop-casted onto a copper grid for TEM Imaging. Atomic Force Microscopy (AFM) measurements were conducted using a Park Systems NX10 instrument.

4.1.2.10 Nuclear Magnetic Resonance (NMR) (¹H, ³¹P).

¹H, and ³¹P NMR spectra were recorded using a 500 MHz Bruker AV500 NMR instrument at 298 K using D₂O as solvent. The NMR analysis was done for GMP, and CA-GMP at similar concentrations to hydrogel (GMP: 125 mM, and CA-GMP 100:125 mM). To study the NMR of the hydrogel, it was converted to a solution state owing to its thermoreversible property and then transferred into the NMR tube, where it turned back to gel state. For ¹H NMR analysis of NH₃ formation was recorded using a 400 MHz Bruker AV400 NMR instrument at 298 K using an H₂O: DMSO-d₆ solvent mixture in a 4:1 ratio and H₂SO₄.

4.1.3 Preparation of GMP-CA (GC) hydrogel

GC hydrogel was prepared by the non-covalent driven self-assembly method. Typically, 1 mL of (250 mM, 101 mg) GMP and (200 mM, 36 mg) CA were prepared separately. The solutions were then mixed in a vial and heated to 50 °C for 4 minutes while stirring gently to promote even interaction. Once heated, the solution was allowed to cool to room temperature naturally, leading to formation of a transparent yellow thermoreversible GC hydrogel.

4.1.4 Preparation of Metal-incorporated GC (GC-M) Hydrogel

Briefly, the GC hydrogel was prepared by using the above procedure and the gel was heated to 50 °C to convert it into sol phase. The appropriate concentration of aqueous solutions of different metal salts (Fe³⁺, Sr²⁺, Cu²⁺, Zr⁴⁺, Mn²⁺, Ca²⁺, Bi³⁺, and Co²⁺) was prepared. The prepared metal solution

was then mixed separately with the GC hydrogel previously heated at 50 °C. After cooling to room temperature, the different hydrogels containing various metal polyphenol complexes were obtained.

In particular, GC-Bi hydrogel was synthesized via the above-discussed method. The concentration of Bi³⁺ was optimized by the addition of an aqueous solution of Bi³⁺ (ranging from 10 mM to 80 mM) to the previously heated GC hydrogel in separate vials and allowed to cool at room temperature. The GC-Bi metallogels at different concentrations of metal salt are obtained.

4.1.5 Preparation of GBi gel

To prepare GBi hydrogel, aqueous solutions of (250 mM, 101 mg) GMP and Bi(NO₃)₃.5H₂O ranging from (10 mM to 80 mM) were freshly prepared. Both solutions were added in vials, and mixture was heated to 50 °C for 2-4 minutes under gentle stirring. After heating, the solution was allowed to cool at ambient room conditions, yielding a white GBi gel.

4.1.6 Preparation of CBi Coordination complex

The CBi complex was synthesized using a simple and efficient method. In a 25 mL round bottom flask, (200 mM, 5 mL) caffeic acid was added and stirred at 65 °C, 500 rpm for 30 minutes to ensure complete solubility, followed by the addition of (80 mM, 5 mL) Bi(NO₃)₃.5H₂O to maintain a molar ratio of 100:40 respectively. The reaction mixture was then stirred vigorously for 2 h to obtain an orange-colored precipitate. The reaction mixture was centrifuged for 10 minutes. The precipitate was separated, washed with water and methanol. The washed precipitate was collected in a petri dish and dried overnight, yielding an orange coloured powdered CBi complex

4.1.7 Thioflavin T (ThT) Binding

A 1 mM stock solution of ThT was initially prepared in ethanol, then diluted to a concentration of 10 μ M using water. The GC and GBi gel was used as

the gel conc. in the 10 μM ThT solution and allowed to incubate for two days.

4.1.8 Photocatalytic nitrogen reduction reaction (PNRR)

Photocatalytic nitrogen fixation experiments were carried out in a 25 mL round-bottom flask. Initially, 20 mg of catalyst and 10 mL of distilled water were introduced into the flask, followed by nitrogen saturation through continuous bubbling of N_2 gas from a balloon for 1 hour. This step ensured effective displacement of dissolved oxygen and saturation of the aqueous phase with nitrogen. The sealed system was then exposed to white light irradiation from a White LED (3 \times 30 W) with stirring at ambient temperature and pressure conditions. After a certain reaction time, liquid products were collected from the reactor, and the catalyst was centrifuged. The NH_3 yield was quantitatively analyzed using Nessler's reagent and the indophenol blue method.

4.1.8.1 Nessler's Reagent Test for NH₄⁺ ion

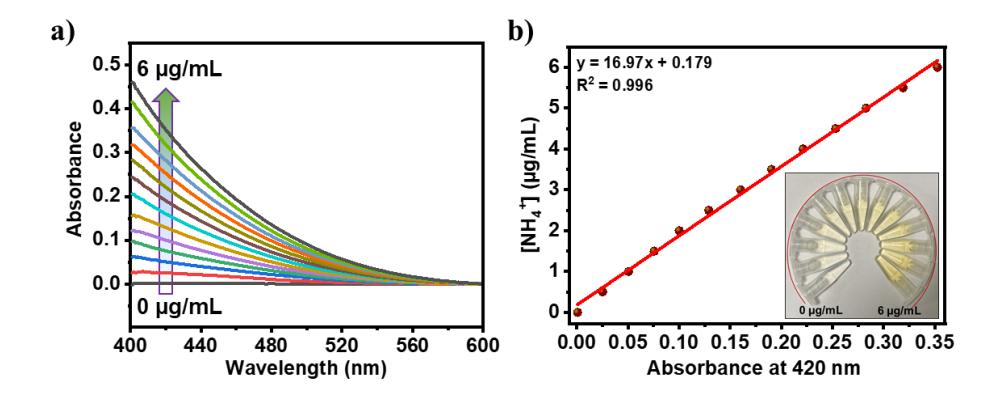


Figure 10. (a) UV-Vis absorption curves of Nessler's reagent assays with various concentrations of NH₄⁺, and (b) A calibration curve for estimating the concentrations of NH₄⁺. (Inset: digital photograph of concentration-dependent complex formation of NH₄⁺ with Nessler's reagent).

The Nessler's reagent test is a widely used method for detecting and measuring ammonium ions (NH⁴⁺) in water samples.¹⁴ This test relies on a chemical reaction where ammonium ions interact with Nessler's reagent

(K_2HgI_4) in an alkaline environment, forming a yellow to brownish complex. The color intensity increases with higher ammonium concentrations, making it possible to determine the concentration using UV-Vis spectroscopy. To perform the test, standard solutions containing different concentrations of ammonium (0–6 μ g/mL) were prepared, mixed with Nessler's reagent, and left to react for 10 minutes. The absorbance was then recorded within the 400–600 nm range, focusing on 420 nm. The results, as shown in Figure 10a, indicate that absorbance at 420 nm increases with ammonium concentration, confirming the formation of the colored complex. Figure 10b presents a calibration curve, demonstrating a strong linear relationship, where y represents ammonium concentration and x is absorbance. The high correlation suggests the test is highly accurate and reliable. Additionally, the inset image in Figure 10b visually represents the color changes from colorless (0 μ g/mL) to deep yellow (6 μ g/mL), further supporting the method's effectiveness.

4.1.8.2 Indophenol Blue Method Test for NH₄⁺ ion

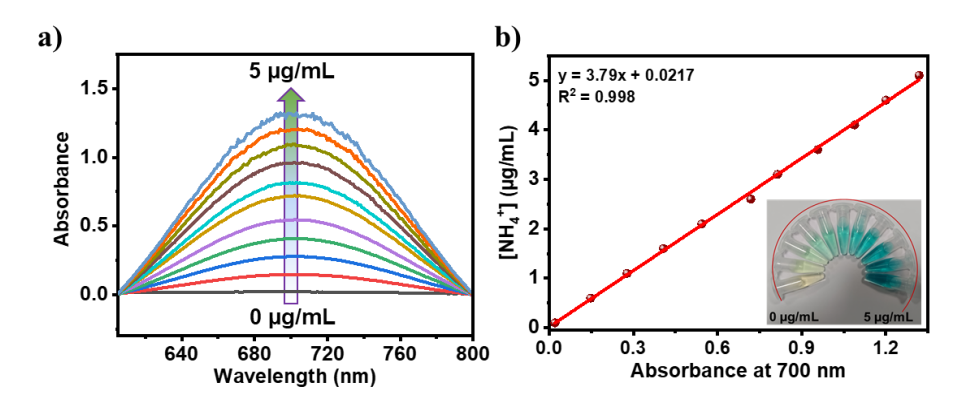


Figure 11. (a) UV-Vis spectra obtained using standard solutions of NH₄Cl after reaction with indophenol blue, and (b) and the resulting linear calibration curve. (Inset: digital photograph of concentration-dependent complex formation of NH₄⁺ with indophenol blue).

This analytical method is based on the reaction of ammonium ions with a chromogenic reagent in the presence of sodium hypochlorite and sodium

nitroprusside, leading to the formation of an indophenol blue complex. The chromogenic reagent was prepared using salicylic acid, sodium potassium tartrate, and sodium hydroxide. The resulting blue coloration, indicative of the indophenol complex, is directly proportional to the ammonium concentration, enabling quantitative analysis via UV-Visible spectroscopy. In this study, a series of standard ammonium solutions ranging from 0 to 5 µg/mL were prepared and subjected to reaction with the chromogenic reagent. The mixtures were incubated to allow complete color development. The absorbance of the resulting solutions was then recorded at 690 nm using a UV-Vis spectrophotometer. A progressive increase in absorbance intensity was observed with increasing ammonium concentrations, confirming the successful formation of the indophenol blue complex (Figure 11a). A calibration curve constructed by plotting absorbance at 690 nm against ammonium concentration exhibited a strong linear correlation, demonstrating the method's high accuracy, reproducibility, and sensitivity (Figure 11b). Additionally, a visual transition from colorless to deep blue with increasing ammonium concentration further supported the quantitative findings.

4.1.8.3 Watt-Chrisp spectrophotometric method for the detection of hydrazine (N₂H₄)

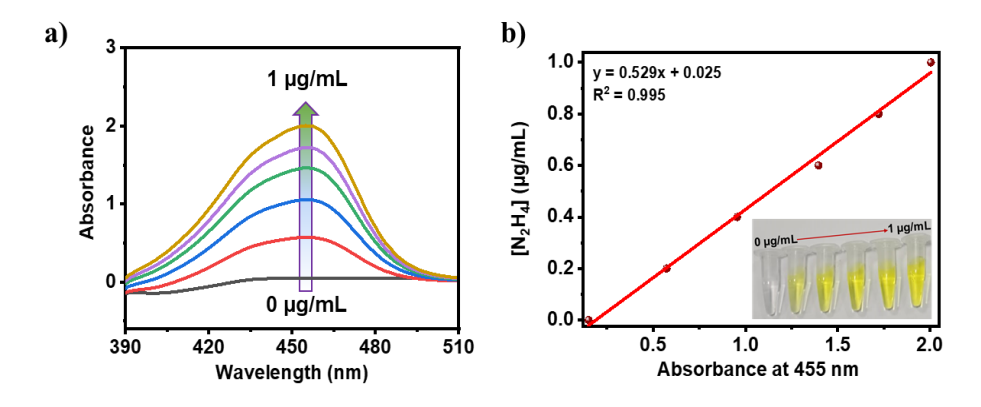


Figure 12. (a) UV-Vis spectra of standard N₂H₄ solutions after reaction with a colorimetric reagent, and (b) the resulting linear calibration curve. (Inset:

digital photograph of concentration-dependent complex formation of N_2H_4).

For the colorimetric detection of hydrazine (N₂H₄), a reagent solution was prepared by dissolving p-dimethylaminobenzaldehyde in a mixture of concentrated hydrochloric acid and ethanol.¹⁴ A fixed volume of this reagent was added to each sample, followed by stirring at room temperature for a defined period to allow complete color development. In this study, a series of standard hydrazine solutions ranging from 0 to 1 µg/mL were prepared and subjected to reaction with the colouring reagent Figure 12a. The absorbance of the resulting solution was then measured using a UVvisible spectrophotometer at 455 nm. The results, as shown in Figure 12b, indicate that absorbance at 455 nm increases with hydrazine concentration, confirming the formation of the colored complex. A standard calibration curve was generated using hydrazine solutions of known concentrations, each diluted with dilute hydrochloric acid prior to reagent addition. All standard and experimental samples were processed and analyzed simultaneously under identical conditions to eliminate variations due to environmental factors.

4.1.8.4 Determination of NO₃ and NO₂ ion

The presence of nitrate ions was assessed using the sulfamic acid method, wherein the prepared reagent was added to the sample solution to eliminate potential nitrite interference. The resulting solution was analyzed at 219 nm using a UV-visible spectrophotometer. No characteristic color change from colorless to yellow was observed, indicating the absence of detectable nitrate ions in the sample. Similarly, the detection of nitrite ions was carried out using the Griess's reagent. The sample was treated under standard conditions, and the formation of a pink-colored azo dye was expected in the presence of nitrite. However, no visible color change occurred, confirming the absence of nitrite ions. Both analyses suggest that the sample is free

from nitrate and nitrite impurities under the given experimental conditions. 14

CHAPTER 5

5.1 RESULTS AND DISCUSSION

5.1.1 Fabrication and Characterization of (GMP-CA) GC Hydrogel

Caffeic acid (CA), a naturally occurring plant-derived polyphenol, comprising phenolic and acrylic functional groups, is known for its significant role in diverse biological and chemical activities. Although it is partially miscible in water, the introduction of GMP at a molar ratio of 1.25:1 led to the formation of a water-soluble, homogeneous self-assembled system, which ultimately resulted in the GMP-CA (GC) hydrogel. In this approach, aqueous dispersion of 200 mM of CA was combined with a 250 mM aqueous GMP solution maintained at physiological pH. The mixture was heated to 50 °C until CA was fully dissolved, yielding a transparent yellow solution. Upon cooling to room temperature, this solution transformed into a uniform self-assembled hydrogel (Figure 13a). The successful formation of the GC hydrogel was confirmed visually using the vial inversion test, where the gel matrix effectively immobilized the solvent even after inversion. This GC hydrogel demonstrated thermoreversible characteristics, transitioning back to a sol state upon heating to 50 °C and reforming the gel structure once cooled to room temperature. The resulting GC gel was further subjected to detailed characterization using various microscopic and spectroscopic techniques.

5.1.1.1 Morphological Evaluation

The structural morphology of the GC hydrogel was examined using various microscopic techniques. FESEM of the dried GC hydrogel cast on a glass plate displayed a network of densely entangled nanofibers, with an average fiber diameter ranging between 70–80 nm (Figure 13b). Additionally, TEM offered insights into the fine structure, showing that thin fibers were crosslinked and bundled together to form larger, intertwined assemblies with

diameters reaching approximately 150–200 nm (Figure 13c). It is likely that individual G-quadruplex strands were extensively cross-linked via noncovalent interactions, which facilitated the development of a bundled and entangled fibrillar network capable of holding substantial amounts of water. AFM further validated the formation of entangled helical fibers, revealing an average fibril height and pitch length in the range of 13-15 nm and 270–300 nm, respectively (Figure 13d).

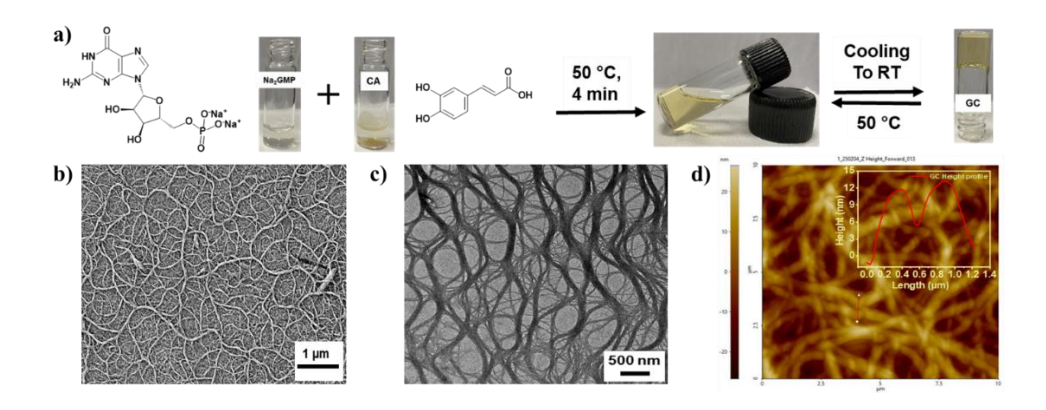


Figure 13. (a) Formation of the GMP-CA hydrogel along with its thermoreversible nature, (b) FESEM image, (c) TEM image, and (d) AFM image of the GC hydrogel (inset: height profile of the fiber morphology).

5.1.1.2 Spectroscopic Characterization

Various spectroscopic methods were employed to gain deeper insights into the polyphenol-driven assembly of GMP and the non-covalent interactions responsible for GC hydrogel formation. UV-visible measurements were performed to examine the alterations in the optical properties of the sample before and after it was subjected to physical stimuli (Figure 14a). UV spectrum of GMP exhibits a sharp peak around 252 nm, characteristic of the π - π * transitions of the purine base in guanosine monophosphate (GMP). The spectrum for CA shows a broader and slightly red-shifted absorbance compared to GMP due to the presence of a carboxylic acid group, with a maximum absorbance around 315 nm, accompanied by a shoulder peak appearing at 290 nm was attributed to π - π * transitions occurring within the conjugated benzene ring and neighboring double bonds, along with n- π *

transitions associated with the lone electron pairs present on the oxygen atoms of the hydroxyl (-OH) and carboxyl (-COOH) groups, respectively. Moreover, the absorption peak at 232 nm corresponded to π - π * transitions confined within the benzene ring. When GMP was introduced into the CA solution, hypsochromic shift of 5 nm from the absorbance of pure CA (315 nm) was observed. Additionally, the peaks at 250 nm and 277 nm appeared with a significant increase in the intensity as compared to the pure GMP and CA, which indicates the non-covalent interactions such as hydrogen bonding and π - π stacking between GMP and CA components within the hydrogel matrix.

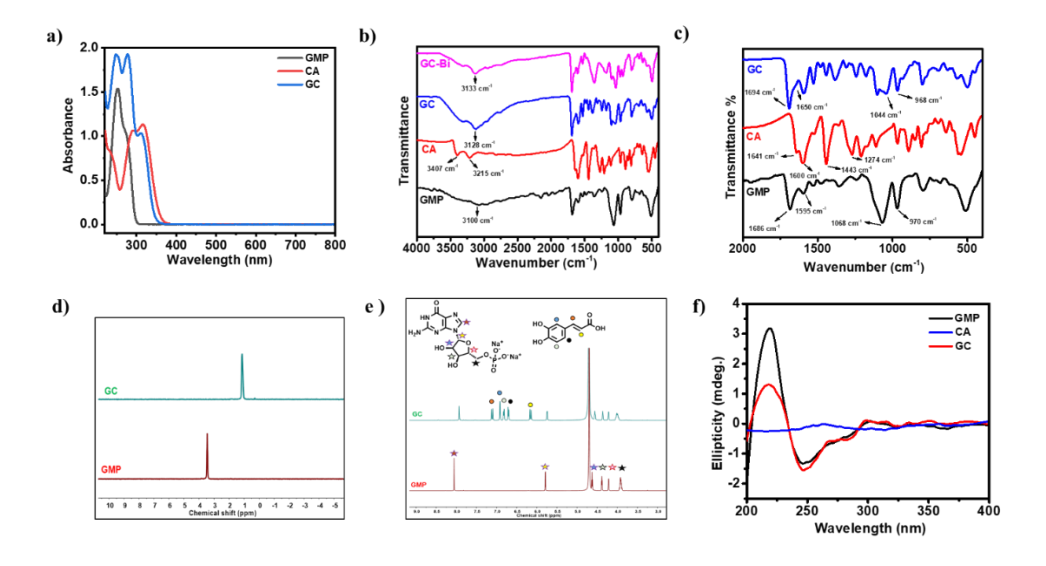


Figure 14. (a) UV–visible spectra of GMP, CA and GC hydrogel, (b) FTIR of GMP, CA and GC xerogel, (c) Zeta potential analysis for GC, GBi and GC-Bi, (d) ³¹P NMR, (e) ¹H NMR of GMP and GC hydrogel, and (f) CD spectra of GMP, CA and GMP-CA hydrogel.

FTIR spectroscopy was conducted to gain insights into the participation of different functional groups in the self-assembly process. (Figure 14c) In case of GMP, the characteristic peak at 1686 cm⁻¹ correspond to C=O stretching, shifted to 1694 cm⁻¹ and the band intensity at 1595 cm⁻¹ assigned to N-H bending, was found to be decrease after hydrogel formation. Additionally, the bands located at 1068 cm⁻¹ and 970 cm⁻¹ in GMP

correspond to asymmetric and symmetric stretching vibrations of the PO₃²bond, respectively. 16 In case of CA, the bands at 1641 cm⁻¹ associated with the C=O group, along with the bands at 3407 cm⁻¹ and 3215 cm⁻¹ corresponds to -OH groups get broadened upon gelation (Figure 14b). These observations indicated that these functional groups actively participated in the non-covalent interactions between GMP and CA, which ultimately facilitated the formation of hydrogel. These interactions were further validated through nuclear magnetic resonance (NMR) analysis of GMP and the GC hydrogel in D₂O. In the ³¹P NMR spectrum (Figure 14d), the phosphate resonance, originally observed at 3.5 ppm for GMP, shifted upfield to 1 ppm after hydrogel formation, suggesting the participation of phosphate groups in hydrogen-bond-assisted cross-linking with CA. (Figure 14e) Similarly, multiple peak shifts in the ¹H NMR spectrum of GMP pointed toward a noncovalent, hierarchical assembly mechanism between GMP and CA, which ultimately resulted in the formation of the GC hydrogel.

Circular dichroism (CD) analysis was performed to illustrate the chiroptical behaviour of the GC hydrogel (Figure 14f). This analysis provides insight into the secondary structure and interactions within these molecular assemblies. In the spectra, GMP alone exhibits a prominent positive Cotton effect at approximately 220 nm, corresponding to an n- π * transition of the purine base, is observed, followed by a noticeable negative peak around 250 nm, indicating the presence of the β -anomeric form of the sugar moieties. These features are characteristic of the right-handed helical stacking of guanosine nucleotides. Upon the introduction of CA to GMP, a modest reduction in ellipticity at the 220 nm peak was observed without significant wavelength shifts. This indicates a potential π - π stacking or hydrogen bonding interactions between purine bases without notable reconfiguration of the GMP's helical arrangement. These observations suggest that CA facilitates self-assembly via non-covalent interactions, while maintaining

the inherent helical structure of GMP, which eventually results in the development of helically arranged chiral fibers within the GC hydrogel.

5.1.1.3 π – π stacking investigation

To investigate the presence of π - π stacking interactions within the selfassembled GC hydrogel, a Thioflavin T (ThT) fluorescence assay was performed (Figure 15a). ThT is known to exhibit a substantial increase in fluorescence intensity upon association with ordered π -stacked domains, thereby serving as a reliable indicator of such molecular arrangements. In its unbound state, ThT shows weak fluorescence at 485 nm when excited at 445 nm, due to the free rotation of its aromatic rings, which leads to nonradiative energy loss. Interestingly, upon introduction into the GC hydrogel environment, ThT displayed an impressive 135-fold enhancement in emission intensity, accompanied by a characteristic red shift of approximately 15 nm. This significant enhancement is attributed to the insertion of ThT molecules into the spaces between stacked G-quartets, leading to an enhanced planar conformation, which restricts its intramolecular rotations and suppresses non-radiative decay pathways. This restricted rotation stabilizes the excited state, allowing for greater fluorescence yield, which is indicative of strong molecular ordering and stacking. The hypsochromic shift in GC is due to the presence of extended conjugation by the carboxylic group of CA. The observed fluorescence behavior was compared with the previous literature reports, strongly supporting the formation of G-quartet motifs, which arise from the hydrogen bonding of four GMP units (Figure S1). These planar G-quartets further assemble via π - π stacking interactions to form higher-order Gquadruplex structures, leading to the fibrillar morphology.

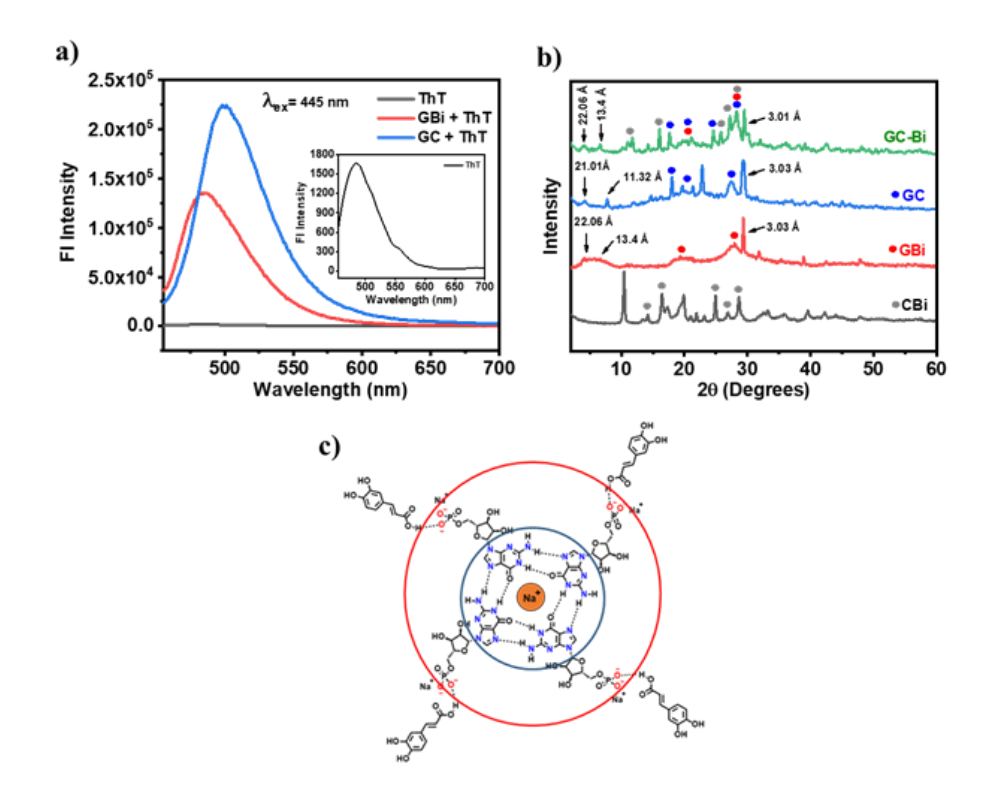


Figure 15. (a) Fluorescence spectra of ThT, GBi + ThT and GC+ThT, (b) PXRD pattern of GC, GBi, GC-Bi and CBi and (c) Plausible structures of G-quartet formation governed by CA.

PXRD was employed to elucidate the structural characteristics and molecular organization within the hydrogel (Figure 15b). The presence of broader, less intense peaks in the diffraction pattern signifies its predominantly amorphous nature. Notably, the two low-angle peaks observed at $2\theta = 4.2^{\circ}$ (d = 21.01 Å) and $2\theta = 7.8^{\circ}$ (d = 11.32 Å) are correspond to the inner and outer shell diameters of an individual G-quartet (Figure 15c), while the peak at $2\theta = 29^{\circ}$ (d = 3.03 Å) represents the interplanar distance between π - π stacked G-quartets, respectively. ^{18,19}

A combination of spectroscopic techniques offers compelling evidence for the proposed mechanism behind the formation of the supramolecular GC hydrogel. Insights gained from circular dichroism (CD), Thioflavin T (ThT) fluorescence assays, and powder X-ray diffraction (PXRD) collectively confirm the existence of G-quartet assemblies within the hydrogel network. Under suitable concentration conditions, guanosine monophosphate (GMP) is capable of spontaneously organizing into G-quadruplex structures through self-assembly. Within a pH window of 3–6, protonation of the phosphate moiety (conversion from PO₃²⁻ to PO₃H⁻) further promotes hydrogen-bonding interactions among the G-quartets, leading to enhanced cross-linking between these supramolecular units. In this system, the protonation process is primarily facilitated by the carboxylic acid functionality of CA, as supported by both ³¹P NMR and FTIR spectral data. This shift in protonation state not only assists in bridging the G-quartet units but also reduces the negative charge density, thereby minimizing electrostatic repulsion and encouraging ordered stacking. In essence, CA plays a crucial role as a molecular cross-linking agent, stabilizing the stacked G-quartet arrays and supporting the growth of a robust, interconnected three-dimensional fibrillar framework.

5.1.1.4 Surface Charge Analysis

In order to investigate the surface charge properties of the fibrillar assemblies, zeta potential analysis was carried out (Figure 17). The GC hydrogel shows a strongly negative zeta potential of around -22 mV, primarily due to the phosphate groups in GMP and catechol groups in CA, which generate significant electrostatic repulsion and enhance stability. The amphiphilic character of guanosine monophosphate (GMP) plays a crucial role in ensuring the uniform dispersion of CA, despite its limited solubility in aqueous environments. This is achieved through a combination of hydrophobic interactions and robust hydrogen-bonding networks. The synergy of these non-covalent interactions directs the CA-assisted self-assembly of GMP, ultimately leading to the development of highly entangled, helical fibrous structures characterized by catechol-functionalized G-quadruplex frameworks.

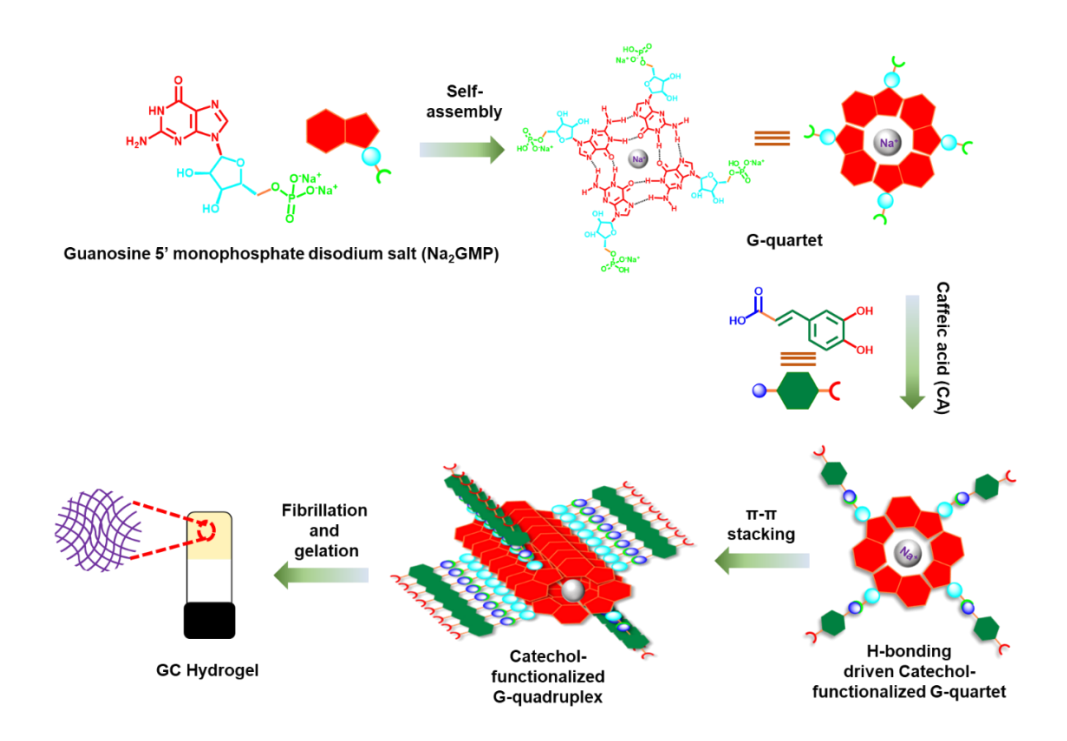


Figure 16. Gelation mechanism of GC hydrogel induced via G-quadruplex formation.

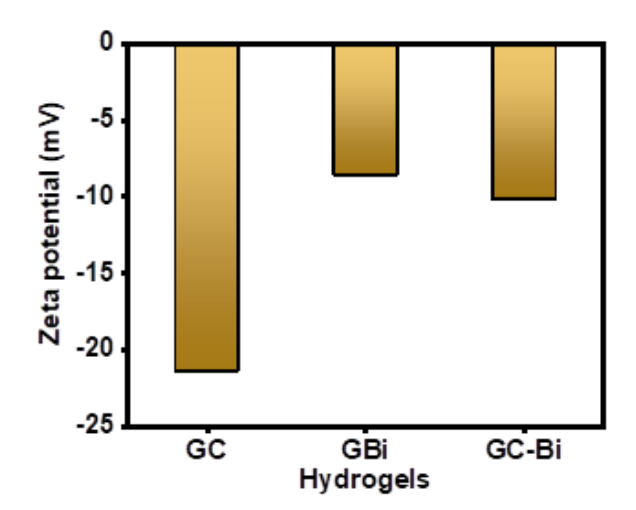


Figure 17. Zeta potential analysis for GC, GBi and GC-Bi hydrogels.

5.1.2 G-quadruplex-based GC Hydrogel: An adoptive Scaffold for Multifunctional Metal ion Integration

The catechol functionalities present on the G-quadruplex framework provide a versatile platform for the direct fabrication of metal–polyphenol coordination complexes on the surface of the fibrillar network. Metal ions, which are abundant in nature, play an essential role in guiding the assembly of functional materials across various scientific fields, including chemistry, biology, and materials science. Their inherent capacity to form stable coordination bonds with polyphenolic ligands enables precise control over molecular arrangement and introduces distinct physicochemical characteristics to the final constructs, rendering them highly valuable in advanced material design.^{20,21}

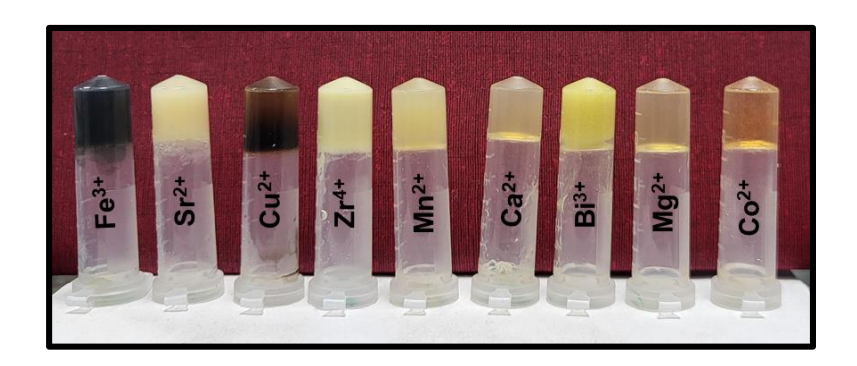


Figure 18. Photographic image of metal ion-induced coordination cross-linking in catechol-functionalized G-quadruplex GC hydrogels.

In this context, the introduction of metal ions not only promotes cross-linking among catechol-functionalized G-quadruplex assemblies but also endows the resulting hydrogels with the specific properties associated with their corresponding metal–polyphenol frameworks. Utilizing the thermoreversible behavior of the GC hydrogel, the system was initially heated to 50 °C to induce the sol phase. Subsequently, aqueous solutions of selected metal salts — including Fe³⁺, Sr²⁺, Cu²⁺, Zr⁴⁺, Mn²⁺, Ca²⁺, Bi³⁺, Mg²⁺, and Co²⁺ — were introduced (Figure 18). Upon cooling the system

back to ambient conditions, the formation of structurally diverse G-quadruplex hydrogels featuring unique metal-polyphenol coordination networks was observed. This strategy offers a straightforward route for tailoring the properties of the hydrogel through the selective incorporation of metal ions, exploiting the broad coordination chemistry of polyphenolic ligands.

5.1.2.1 Strategic Incorporation of Bismuth for Functional GC-Bi Hydrogel Engineering

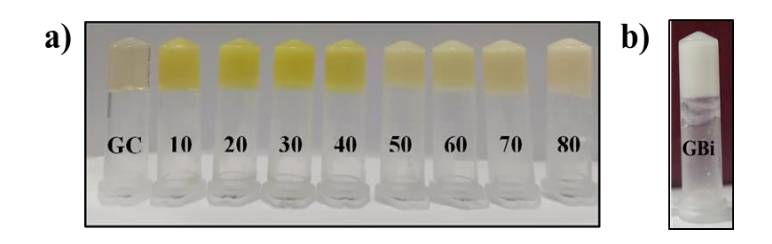


Figure 19. (a) Varying the conc. (mM) of Bi³⁺ keeping the conc. of GMP (125 mM) and CA (100 mM) constant, (b) GBi hydrogel at 125:40 mM conc. respectively.

Bismuth-based semiconductors have emerged as promising candidates for photocatalytic applications, owing to their desirable combination of environmental compatibility, cost-effectiveness, high stability, and strong absorption in the visible-light region. Their suitable band gaps and efficient charge separation capabilities make them particularly effective in processes such as CO₂ reduction, organic pollutant degradation, solar energy conversion, and photoelectrochemical reactions. ^{22,23} Inspired by these advantages, a bismuth-polyphenol complex (CBi) was purposefully embedded within the G-quadruplex hydrogel matrix, resulting in a hybrid material, termed GC-Bi, specifically designed for photocatalytic nitrogen reduction (PNRR). This integration not only utilizes the intrinsic photocatalytic activity of bismuth but also benefits from the adaptable and supportive architecture of the G-quadruplex network, establishing an

efficient and stable platform for ammonia production under ambient conditions.

The GC-Bi hydrogel was optimized by systematically adjusting the Bi³⁺ ion concentration from 10 mM to 80 mM within the GC matrix. Hydrogels formed successfully at all tested concentrations. Initially, the GC hydrogel clear and transparent, indicating no metal presence (Figure 19a). With the introduction of metal ions at low conc. (10 to 40 mM), the yellow color intensifies as the concentration increases reflecting stronger coordination interactions between the Bi³⁺ and the catechol groups of CA. Upon further increase in metal concentration (50 mM and above), the gel turns white, suggesting a dense packing of metal ions within the gel, possibly interacting with specific groups like phosphate in GMP, altering the optical properties of the hydrogel. A consistent trend was observed in UV–visible spectra (Figure S2), with absorbance in the visible range intensifying from 10 mM to 40 mM, followed by a sharp reduction at higher concentrations.

Rheological studies revealed that the mechanical strength of the hydrogels progressively increased with the concentration of Bi³⁺, reaching its maximum at 30 mM, beyond which no significant enhancement was observed. Considering both the mechanical properties and optical clarity, a Bi³⁺ concentration of 40 mM was determined to be optimal for the GC–Bi hydrogel formulation and was employed for further characterization and functional assessments (Figure S3). To better understand the role of each component, control experiments were performed by mixing aqueous Bi³⁺ solutions individually with GMP and CA, keeping the molar ratio consistent with that of the GC–Bi hydrogel system (GMP:CA:Bi = 125:100:40). Notably, the mixture of GMP and Bi³⁺ alone led to the formation of a thermoreversible hydrogel, hereafter referred to as GBi hydrogel (Figure 19b). Conversely, the combination of CA and Bi³⁺ produced an orange-hued coordination complex precipitate, denoted as the CBi complex.

5.1.2.2 Morphological Evaluation of GC-Bi, GBi and CBi

The structural morphology of the GC-Bi and GBi hydrogels was examined using various microscopic techniques to assess the influence of bismuth ion incorporation on the self-assembled network (Figure 20a, e). FESEM of the dried GC-Bi and GBi hydrogels displayed helical morphology with an average fiber diameter ranging between 70-80 nm, comparable to that observed in the GC hydrogel (Figure 20b, f). Energy-dispersive X-ray (EDX) spectroscopy validated the successful incorporation of Bi³⁺ ions into the fibrillar architectures, with C, N, O, P, Na, and Bi elements identified in both GC-Bi and GBi systems. Elemental mapping revealed a uniform distribution of these elements across the fibrillar structures, confirming their homogeneous integration (Figure S4 and S5). TEM further confirmed the presence of well-defined fibrillar structures in both GC-Bi and GBi hydrogels, reflecting the formation of an ordered and continuous network throughout the matrix with diameters reaching approximately 150–200 nm (Figure 20c, g). The introduction of bismuth ions is likely to promote enhanced crosslinking via ionic interactions, which contributes to the observed structural integrity. AFM additionally validated the formation of helical fibrillar assemblies, revealing an average fibril height of approximately 7–9 nm for GC-Bi and 5–7 nm for GBi, while the pitch length was found to be in the range of 260-280 nm (Figure 20d, h). These observations suggest that the presence of Bi³⁺ reinforces the supramolecular architecture, resulting in a more cohesive and stabilized hydrogel network.

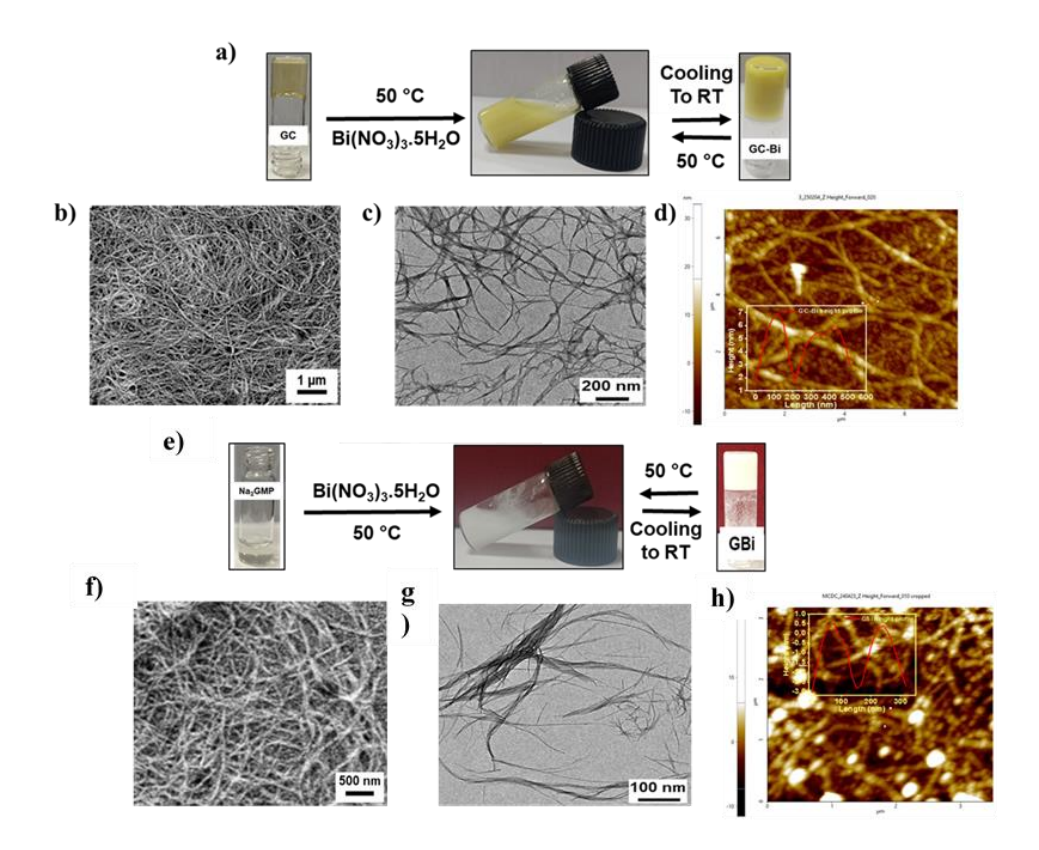


Figure 20. (a) Formation of the GC-Bi hydrogel along with its thermoreversible nature, (b) FESEM image, (c) TEM, and (d) AFM images of the GC-Bi hydrogel, (e) Formation of the GBi hydrogel along with its thermoreversible nature, (f) FESEM, (c) TEM, and (d) AFM images of the GBi hydrogel.

To further investigate and compare the properties of the free bismuth–polyphenol complex with its hydrogel-incorporated counterpart, the CBi complex was independently synthesized. For this, an aqueous solution of bismuth nitrate (80 mM) was gradually introduced into a CA solution (200 mM) under stirring, resulting in the formation of an orange-colored precipitate (Figure 21a). The obtained solid was isolated, dried, and subjected to detailed morphological and compositional analysis. FESEM revealed that the CBi complex exhibits a characteristic peanut-shaped morphology (Figure 21b). Energy-Dispersive X-ray Spectroscopy (EDX) analysis confirmed the presence of carbon (C), bismuth (Bi), and oxygen

(O) within the sample, which demonstrated a uniform spatial distribution of these elements across the entire structure (Figure 21c). Furthermore, FTIR analysis indicated a broadening and noticeable decrease in the intensity of the characteristic catechol –OH stretching bands at 3397 and 3217 cm⁻¹ in pure C, suggesting the successful coordination between the catechol moieties and Bi³⁺ ions within the complex (Figure 21d).

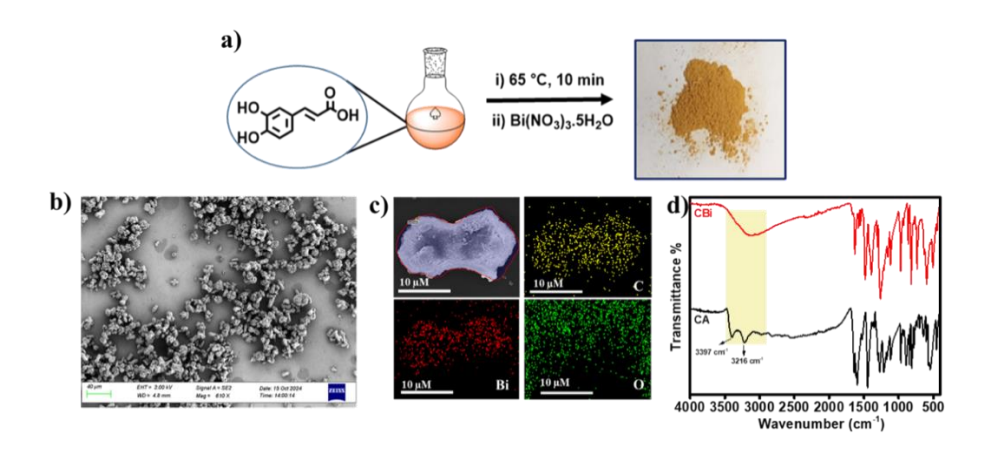


Figure 21. a) Synthetic scheme, b) FESEM image, c) EDX elemental mapping of C, Bi, and O, and d) FT-IR spectra of CBi complex.

5.1.2.3 Spectroscopic Characterization

Following the morphological evaluation of the CBi, GBi, and GC-Bi systems, a series of spectroscopic investigations were undertaken to elucidate the nature of interactions between Bi³⁺ ions and the components of the G-quadruplex hydrogel, and their influence on the self-assembly behavior. The UV-Vis absorption spectrum (Figure 22a) of GBi exhibited a maximum in the ultraviolet region, closely aligning with the spectral profile of unmodified GMP, thereby indicating that the coordination of Bi³⁺ ions does not significantly alter the electronic environment of the guanine moiety. In contrast, the spectrum of the CBi complex revealed a markedly broadened absorption band extending into the visible region, which is attributed to metal-ligand charge transfer interactions between Bi³⁺ ions and the catechol functionalities of caffeic acid. Interestingly, the GC-Bi hydrogel displayed the most extensive spectral broadening, with a well-

defined absorption edge near 450 nm. This behavior is indicative of enhanced electronic delocalization, likely due to the synergistic coordination among GMP, caffeic acid, and bismuth ions within the spatial confinement of the fibrillar hydrogel network. Such confinement not only stabilizes the integrated metal—polyphenol complex but also promotes an extended conjugated architecture, thereby enhancing visible-light responsiveness and confirming the successful embedding of the bismuth—polyphenol complex into the G-quadruplex hydrogel matrix.

To further investigate the molecular interactions governing the coordination and confinement of bismuth within the hydrogel matrix, Fourier-transform infrared (FT-IR) spectroscopy was employed. In the GC-Bi hydrogel, a substantial reduction in the intensity of the broad O-H stretching band around 3133 cm⁻¹ was observed (Figure 22 b), indicating the coordination of catechol hydroxyl groups of caffeic acid with Bi3+ ions. In the native GMP spectrum, characteristic peaks were identified at 1686 cm⁻¹ (C=O stretching), 1595 cm⁻¹ (N-H bending), and at 1068 cm⁻¹ and 970 cm⁻¹, corresponding to the asymmetric and symmetric stretching vibrations of the phosphate (PO₃²⁻) moiety (Figure 22c). These peaks exhibited noticeable shifts in the GC-Bi spectrum, signifying the involvement of these functional groups in non-covalent interactions, likely mediated by metal coordination and hydrogen bonding under spatial confinement. Additionally, in the GBi system, the asymmetric phosphate stretching band was significantly shifted to 1036 cm⁻¹, suggesting a strong ionic interaction between the PO₃²⁻ group of GMP and Bi³⁺ ions (Figure 22e). The appearance of a new absorption band around 638 cm⁻¹ across both GBi and GC-Bi samples further supports the formation of Bi-O coordination bonds, confirming successful integration of the metal ion into the hydrogel framework.²⁴

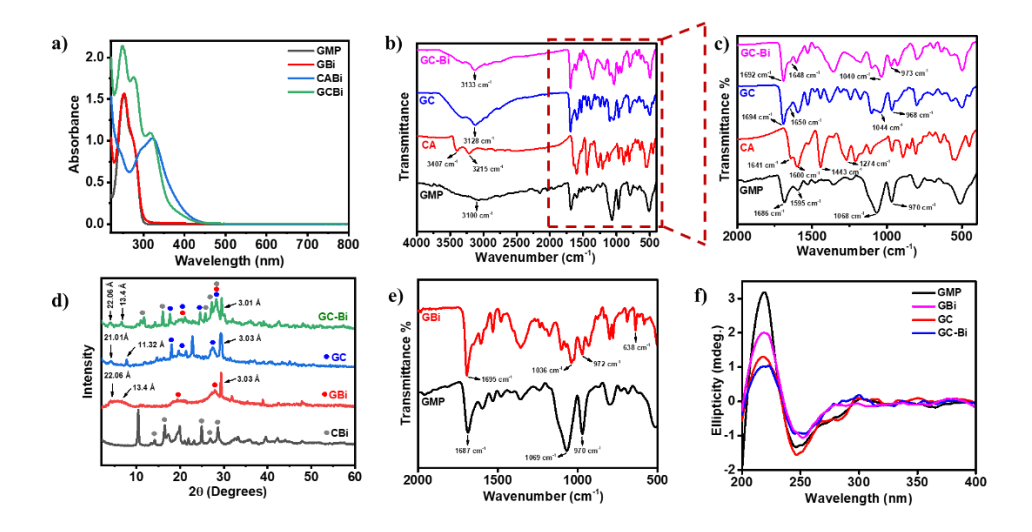


Figure 22. (a) UV-Vis absorption spectra of prepared samples with respect to GMP, (b, c) FTIR spectra of GC-Bi with respect to their components, (d) PXRD pattern of prepared samples, (e) FT-IR spectra of GMP and GBi, (f) and CD spectra of prepared samples with respect to GMP.

To gain further insight into the structural evolution and crystalline behavior following the incorporation of bismuth ions, PXRD analysis was carried out for the CBi complex, GBi, and the GC-Bi hydrogel (Figure 22d). The CBi complex exhibited well-defined, sharp diffraction peaks, indicative of a highly crystalline structure. This pronounced crystallinity can be attributed to the ordered coordination network formed between caffeic acid and Bi3+ ions in the absence of guanosine-based confinement. In contrast, both GBi and GC-Bi displayed significantly broader and less intense peaks, reflecting a predominantly amorphous character. This reduction in crystallinity suggests that the spatial confinement and supramolecular interactions within the G-quadruplex framework hinder the formation of long-range ordered domains typically observed in the standalone CBi complex. Notably, the characteristic low-angle reflections at 4.2° and 7.8°, corresponding to the inner and outer diameters of the guanine quartet channels, were preserved in GBi and GC-Bi. However, a distinct shift in the inner shell reflection implies partial substitution of monovalent cations

(e.g., Na⁺) by Bi³⁺ within the G-quartet cavity, leading to enhanced structural stabilization (Figure 23a, b). Moreover, GC-Bi also retains some peaks from the CBi complex, indicating its properties are incorporated into GC-Bi without preserving the original complex, resulting in a unique hybrid material.

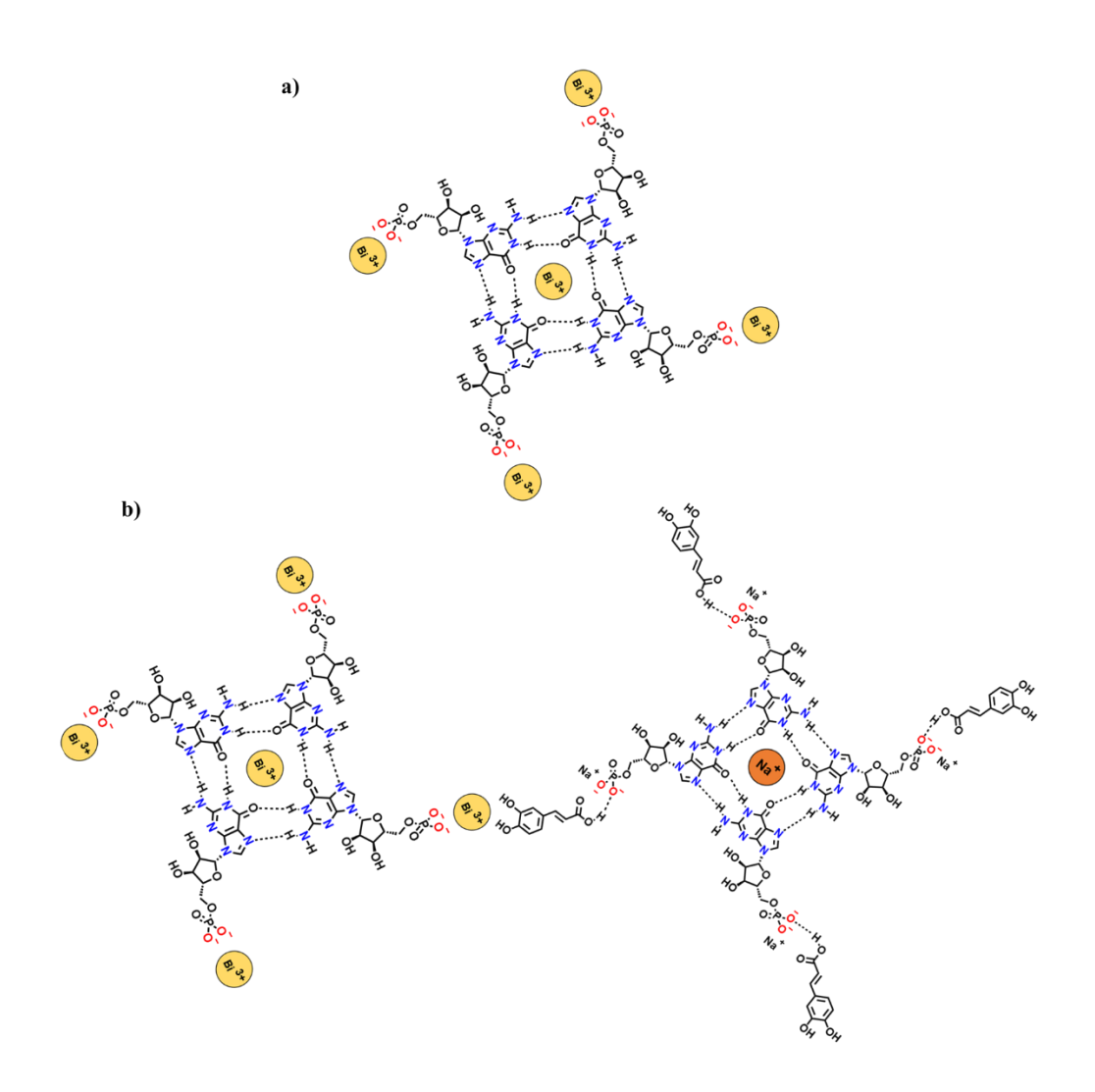


Figure 23. Plausible structures of G-quartet formation governed by (a) Bi³⁺ and (b) cross-linking of G-quartets obtained by GC and GBi.

Circular Dichroism (CD) spectroscopy was utilized to examine the influence of Bi³⁺ on the chiral self-assembly behavior of GMP and GC.

Notable changes were observed in the CD spectra of both GBi and GC-Bi upon Bi³⁺ addition, including the disappearance of a negative shoulder at 285 nm and reduced ellipticity at 250 and 220 nm, indicating conformational rearrangements (Figure 22f). To investigate this phenomenon further, a concentration-dependent CD analysis was conducted by varying Bi³⁺ concentrations (0.1–0.5 mM) while maintaining GMP at 0.5 mM. The negative shoulder at 285 nm progressively diminished with increasing Bi³⁺ concentration up to 0.2 mM, after which a positive Cotton effect emerged at the same wavelength, along with an increase in ellipticity (Figure S6). These findings suggest that Bi³⁺ drives a conformational transition in GMP, facilitating the formation of antiparallel G-quadruplex assemblies and resulting in well-ordered quadruplex superstructures.

5.1.2.4 Band Gap Calculation using Tauc's Plot

The photographic images illustrate the physical appearance of the synthesized materials, GBi as a fibrous white solid, CBi as a vibrant orange powder, and GC-Bi as a pale yellow xerogel (Figure 24a). These visual differences reflect variations in molecular composition and structural arrangement, highlighting the need for optical characterization to assess their electronic properties. The absorption edge for GBi appears at approximately 365 nm, suggesting limited absorption in the visible range. In contrast, CBi displays a red-shifted edge around 460 nm, indicative of an extended π-conjugation resulting from coordination between caffeic acid and Bi³⁺. Notably, GC–Bi exhibits the most pronounced red shift with an absorption edge near 450 nm, implying synergistic interactions among GMP, caffeic acid, and bismuth within the hydrogel network, leading to enhanced visible light absorption (Figure 24b).

To quantitatively determine the optical band gaps of these materials, Tauc plots were constructed using the absorption data. The Tauc's relation is given by the equation:

$$(\alpha h v)^n = A(h v - Eg)$$

where α is the absorption coefficient, hv is the photon energy, A is a constant, Eg is the optical band gap, and n is the exponent that depends on the nature of the electronic transition (with n=1/2 for allowed direct transitions). As shown in Figure c, the extrapolation of the linear regions of the Tauc plots yields band gap values of 3.5 eV for GBi, 2.7 eV for CBi, and 2.75 eV for GC-Bi. These results underscore the significant reduction in band gap upon incorporating the CBi complex into the G-quadruplex hydrogel, highlighting the role of the confined hydrogel environment in facilitating enhanced visible light absorption (Figure 24c). The intermediate band gap of GC-Bi relative to its individual components suggests a unique hybridization of electronic states, providing a promising platform for photocatalytic applications.

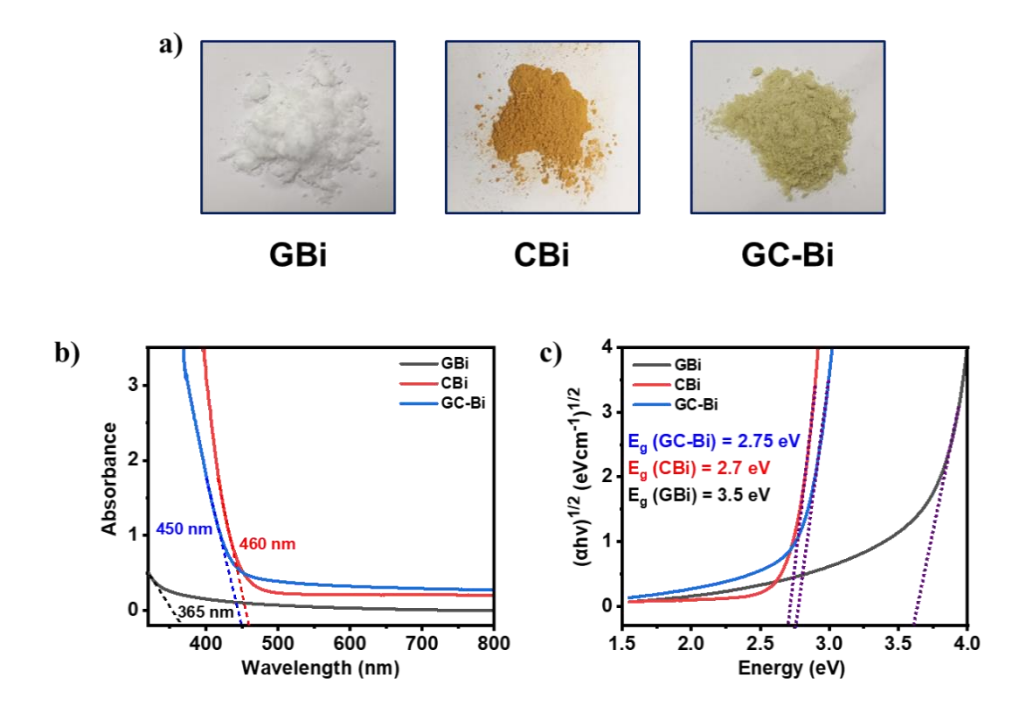


Figure 24. (a) Photographic images of powdered GBi, CBi and GC-Bi, (b) UV-Vis spectra, (c) and Band Gap Calculations using Tauc's Plot of GBi, CBi and GC-Bi.

5.1.3 Photocatalytic Nitrogen Reduction Reaction (PNRR)

Photocatalytic conversion of dinitrogen (N₂) to ammonia (NH₃) under ambient conditions presents a compelling approach toward sustainable nitrogen fixation. In this context, the metal–polyphenol-based hybrid materials synthesized in our study demonstrate significant potential for catalytic nitrogen fixation. The investigation was centered around three catalyst systems: CBi, GBi, and GC-Bi. A systematic evaluation of these materials was conducted under simulated light irradiation to assess their ammonia (NH₃) generation capabilities.

As illustrated in Figure 25a, photocatalytic nitrogen fixation was performed using the synthesized CBi, GBi, and GC-Bi catalysts in aqueous media under ambient temperature and pressure. The ammonia concentration was quantified using Nessler's reagent with UV–Vis spectroscopy at 420 nm and indophenol blue method with . Among the three systems, the GC-Bi

composite yielded a maximum ammonia production of 905.2 μmol g⁻¹ h⁻¹, which was nearly four times higher than that observed for the CBi catalyst. To further optimize the GC-Bi catalyst, varying concentrations of Bi³⁺ (10–50 mM) were employed to examine their influence on ammonia production (Figure 25b). The results clearly demonstrate a concentration dependent trend, wherein the ammonia yield peaked at 40 mM Bi³⁺ loading. This indicates an optimal ratio of metal to organic ligands where the coordination environment and porosity are favorably balanced. At lower Bi³⁺ concentrations, insufficient catalytic active sites are available, while at higher concentrations, the excess bismuth ions may induce particle agglomeration or excessive precipitation, reducing the catalytic surface area. A series of control experiments were performed to verify the photocatalytic origin of the ammonia generation (Figure 25c). No detectable NH₃ was observed under the following conditions: (i) in the absence of N₂ (Ar atmosphere), (ii) in the dark, (iii) in the absence of catalyst.

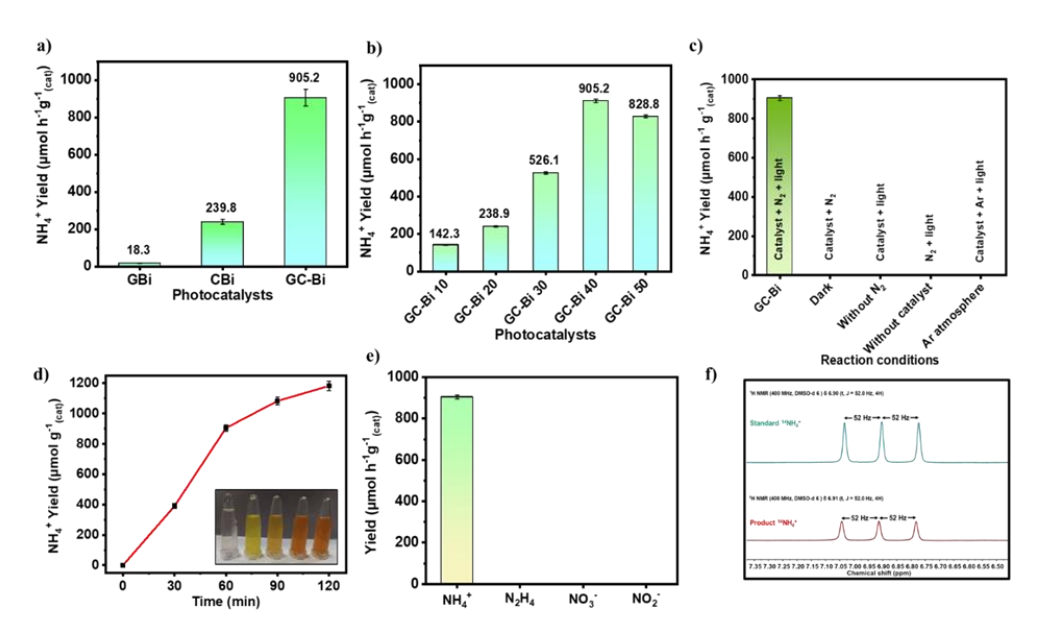


Figure 25. (a) The NH₄ $^+$ yield using prepared catalysts under white light irradiation in N₂, (b) Effect of bismuth ion concentration (10–50 mM) on NH₄ $^+$ yield for GC-Bi catalysts, (c) Nitrogen fixation performance through controlled experiments, (d)The NH₄ $^+$ production rates using GC-Bi as a

photocatalyst, (e) selective production of NH_3 , (f) 1H NMR of standard NH_3 and produced NH_3 .

These results confirm that the ammonia generation is strictly dependent on the presence of light, N₂ gas, and the GC-Bi catalyst, thus affirming the photocatalytic NRR mechanism and establishing GC-Bi as the primary driving force in the N₂ reduction process. To understand the kinetics of photocatalytic NRR over GC-Bi, the time-resolved production of ammonia was monitored under constant irradiation (Figure 25d). The results indicate a steady increase in NH₃ concentration within the first 3 hours, beyond which the system attains a saturation point. This behavior is consistent with efficient photocatalytic systems where the catalytic rate stabilizes due to limited available active sites.

To evaluate product selectivity, potential side products including hydrazine (N₂H₄), nitrate (NO₃⁻), and nitrite (NO₂⁻) were analyzed using appropriate colorimetric and spectrophotometric methods. As represented in (Figure 25e), the GC-Bi catalyst demonstrated negligible generation of undesired byproducts, indicating high selectivity toward NH₃ formation. This is essential for practical application, as selective ammonia synthesis without secondary nitrogen-containing species is critical to ensure catalytic efficiency and avoid interference during product quantification.

¹H nuclear magnetic resonance (NMR) spectroscopy was employed to confirm the formation of ammonium ions (NH₄⁺) after photocatalytic nitrogen fixation (Figure 25f). A standard solution of ammonium chloride (NH₄Cl) was first recorded as a reference. To suppress hydrogen exchange and sharpen the ammonium signal, dilute sulfuric acid (H₂SO₄) was added to the samples. DMSO-d6 was used as the solvent to provide a stable lock signal and minimize background interference. In the ¹H NMR spectra, a characteristic triplet signal for NH₄⁺ was observed. ²⁶ This splitting arises due to coupling between the hydrogen nuclei and the nitrogen-14 nucleus (¹⁴N), which has a nuclear spin quantum number (I) of 1. According to the

formula 2nI + 1 (where n = 1 for one neighboring nitrogen), the expected multiplicity is three, resulting in the observed triplet pattern. The position and splitting of the signal matched well with the NH₄Cl standard, confirming successful ammonia generation.

After completing three catalytic cycles, the photocatalytic efficiency reduced to 49% (Figure S7). So to understand the mechanism behind the activity, the catalyst was thoroughly washed with methanol, dried, and subsequently characterized to assess its structural and morphological stability. FESEM and PXRD analyses revealed no significant changes in the surface morphology or crystalline structure, confirming the catalyst's robustness (Figure S8). However, the Bi 4f X-ray Photoelectron Spectroscopy (XPS) spectra exhibited a shift toward higher binding energy for the peaks corresponding to the +3 oxidation state of bismuth. This shift may be attributed to partial oxidation of Bi during the nitrogen reduction reaction to ammonia, indicating a slight decline in catalytic efficiency over repeated cycles. Nevertheless, the observations affirm the heterogeneous nature, structural integrity, and recyclability of GC–Bi throughout the catalytic process.

5.1.4 Exploration of Factors Governing High Ammonia Yield

Achieving efficient photocatalytic nitrogen fixation under ambient conditions necessitates a comprehensive understanding of the fundamental factors that govern catalytic performance. Previous studies have shown that several key parameters critically influence the overall activity of photocatalysts. Among these, a high specific surface area is essential to provide an abundance of accessible active sites for nitrogen adsorption and activation. An optimal band gap within the visible light region, typically between 1.8 and 2.8 eV, ensures efficient solar light utilization while maintaining sufficient redox potentials to drive the multi-electron nitrogen reduction process.

Moreover, the suppression of electron-hole recombination is a decisive factor in enhancing catalytic efficiency. Prolonged carrier lifetimes facilitate effective charge transfer to adsorbed nitrogen species, thereby promoting ammonia generation. Surface engineering strategies, such as heteroatom doping, defect creation, and the construction of heterojunctions, have also been extensively employed to improve photocatalyst performance by tuning the band structure, modulating charge carrier dynamics, and introducing new active sites. These modifications help in enhancing the separation and migration of charge carriers, reducing recombination rates, and increasing the intrinsic reactivity of the catalyst.²⁷

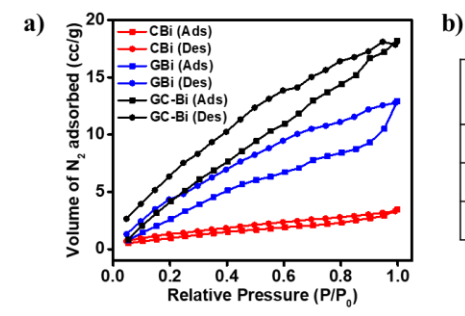
In this study, we systematically investigated these factors to understand their individual and collective influence on photocatalytic ammonia synthesis. Detailed analysis of surface area, band gap position, electron-hole recombination behavior, and surface structural features was carried out to establish a correlation between the material properties and catalytic performance. This approach provides critical insights into the design principles required for developing next-generation photocatalysts for sustainable nitrogen fixation.

5.1.4.1 Thermal Stability and Surface Area Analysis

Thermal stability is a critical parameter for evaluating the structural integrity and practical applicability of catalysts under operating conditions. Thermogravimetric analysis (TGA) provides valuable insights into material stability, purity, and composition (Figure S9). The initial increase in weight observed in the TGA profiles is attributed to the adsorption of N₂ gas. Among the catalysts, CBi exhibits the highest thermal stability, with only gradual mass loss up to 800°C. In contrast, GBi and GC-Bi display more rapid decomposition, particularly GC-Bi, which shows approximately 60% mass loss by 600°C, indicating a higher content of organic or volatile species. This differentiation in thermal stability is crucial for selecting and

tailoring catalysts for specific industrial applications, particularly in temperature-sensitive processes.

The Brunauer-Emmett-Teller (BET) method is widely employed to determine the specific surface area of porous materials, utilizing nitrogen adsorption-desorption isotherms to derive key insights into surface texture, pore structure, and volume. This surface analysis holds particular significance in catalysis research, where the extent of surface exposure and porosity directly influences the density of active sites, mass transport properties, and overall catalytic efficiency. The nitrogen adsorptiondesorption isotherms recorded for the GC-Bi and GBi catalysts exhibit a distinct hysteresis loop, indicative of mesoporous characteristics and the presence of well-organized pore structures (Figure 26a). BET analysis revealed that among the synthesized catalysts, GC-Bi demonstrated the highest specific surface area of 64.433 m²/g (Figure 26b), along with the largest pore volume of 0.026 cc/g and an average pore diameter of 3.440 nm (Figure S10). The larger surface area and mesoporous network of GC-Bi facilitate improved nitrogen adsorption and mass transport, thereby providing more active sites for nitrogen activation and significantly enhancing the photocatalytic ammonia production efficiency.



Catalyst	Surface Area (m²/g)	Pore Size (nm)	Pore Volume (cc/g)
CBi	4.392	3.082	0.004
GBi	19.926	3.079	0.017
GC-Bi	64.433	3.440	0.026

Figure 26. (a) N₂ Adsorption-desorption curves of CBi, GBi and GC-Bi, (b) Comparison of pore size, specific surface area, and pore volume for CBi, GBi, and GC-Bi catalysts.

5.1.4.2 In-Situ Formation of Heterojunction and Oxygen Vacancies

BET surface area analysis and thermogravimetric studies demonstrated that the GC-Bi composite exhibits both an enhanced specific surface area and superior thermal stability compared to its individual constituents, CBi and GBi, facilitating higher active site availability and robust framework integrity. These structural and compositional attributes were further substantiated through detailed X-ray photoelectron spectroscopy (XPS) investigations. The XPS survey spectra confirmed the presence of all the expected elemental peaks corresponding to the CBi, GBi, and GC-Bi. Further, to study the chemical state and electronic environment of Bi in the synthesized materials, Bi 4f spectra were analyzed and compared. In the case of the CBi sample, two well-defined peaks were observed at binding energies of 159.46 eV and 164.82 eV, corresponding to Bi $4f_7/2$ and Bi $4f_5/2$, respectively (Figure 27a). ²⁸ The energy separation between these two peaks is approximately 5.2 eV, which is consistent with the expected spin-orbit coupling for Bi in the +3 oxidation state. The clear presence of Bi³⁺ is indicative of the formation of a stable metal-organic coordination environment in the C-Bi complex, where Bi is predominantly coordinated through oxygen donor atoms of the polyphenolic ligand. When examining the GBi system, the Bi $4f_{7/2}$ and $4f_{5/2}$ peaks appear at slightly lower binding energies, specifically at 159.25 eV and 164.43 eV, respectively. This marginal shift of approximately 0.2 eV towards lower binding energy, while maintaining a consistent spin-orbit splitting of ~5.18 eV, reaffirms that Bi remains in the +3 oxidation state in the GBi network as well. However, the lower binding energy suggests an increased electron density around the Bi centers, likely resulting from electron-donating interactions originating from the guanosine-derived gel matrix. The delocalized π -electron system and possible hydrogen-bonded network in the gel may facilitate partial electron donation to Bi, thereby reducing the effective nuclear charge felt by the core electrons. Strikingly, in the GC-Bi hybrid system, the Bi 4f₇/₂ and 4f₅/₂ peaks are observed at 159.37 eV and 164.67 eV, respectively, lying

precisely between the corresponding peaks of CBi and GBi. The spin-orbit separation remains at ~5.3 eV, once again confirming the oxidation state of bismuth as +3. This intermediate position of the binding energies strongly suggests the coexistence of two distinct chemical environments for bismuth, reflective of an efficient electronic interaction at the interface of the CBi and GBi domains. The observed electronic configuration implies that charge redistribution has occurred across the GC-Bi interface, giving rise to a well-integrated type-1 heterojunction facilitating efficient electron delocalization from GBi (electron-rich) to CBi (electron-deficient) components.²⁹ (Figure 27b) The high-resolution P 2p spectra revealed spinorbit components corresponding to P 2p₃/₂ and P 2p₁/₂ at binding energies of ~132.5 eV and ~133.0 eV, respectively, attributable to the phosphate (PO₄³⁻) group of GMP. Notably, these peaks were positively shifted by approximately 1.0 eV in both GBi and GC-Bi samples relative to GMP, implying a stronger interaction between the phosphate species and the metal center or catechol groups of caffeic acid in the gel-derived systems.

To gain deeper insights into the oxygen chemical environment and defect structure within the synthesized systems, the O 1s spectra were deconvoluted and analyzed (Figure 27c). The spectra exhibited three well-resolved peaks centered at approximately 529.7 eV, 531.1 eV, and 532.4 eV, corresponding to lattice oxygen (OL), oxygen vacancies (OV), and surface hydroxyl groups (OH), respectively. In both GBi and GC-Bi systems, all three oxygen species were distinctly present, whereas the CBi spectrum notably lacked the OH component entirely, indicating the absence of significant surface-bound hydroxyl functionalities in the catechol–bismuth complex.

The lattice oxygen peak (OL), observed at ~529.7 eV, is primarily attributed to metal-oxygen bonding environments such as Bi-O-C and P-O linkages that constitute the structural backbone of the composite. Meanwhile, the OV peak at ~531.1 eV corresponds to oxygen-deficient regions, including non-

bridging oxygen atoms and P=O or C=O moieties introduced during gel formation. The OH component, centered on 532.4 eV, reflects adsorbed water or bridging hydroxyl groups typically associated with gel matrices or surface hydration layers.³⁰

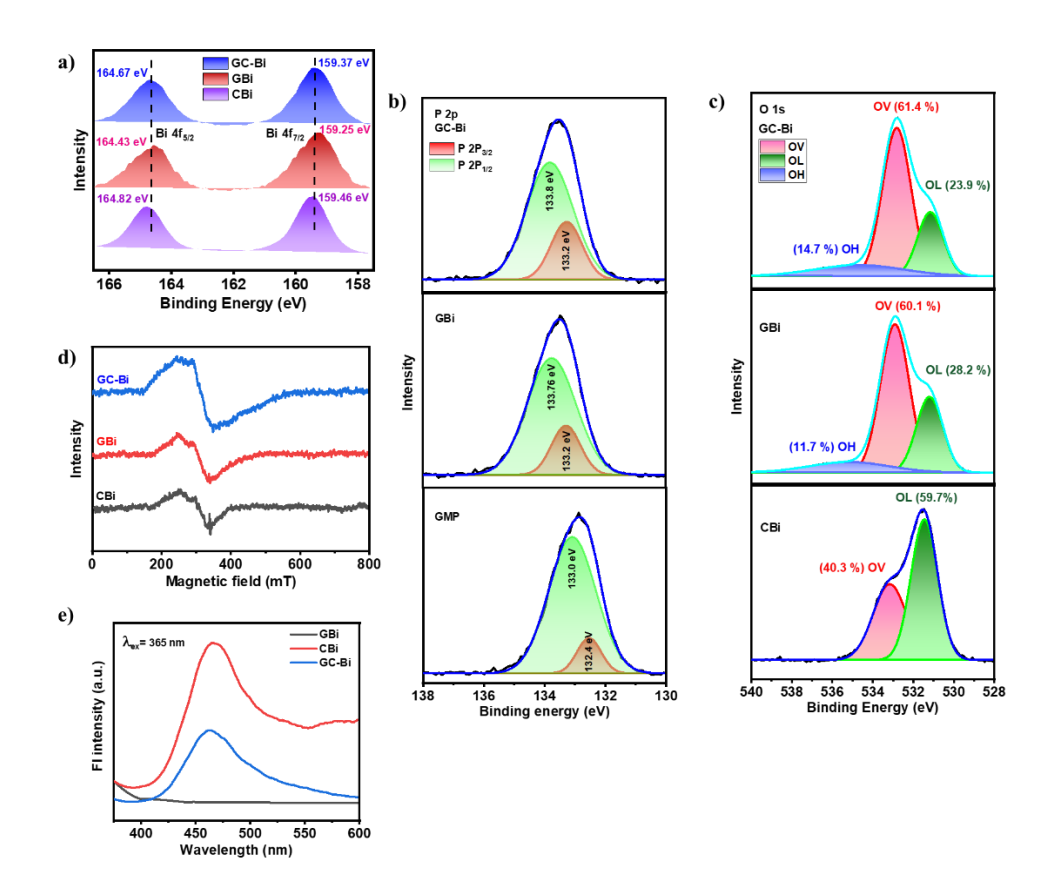


Figure 27. (a) Bi 4f, (b) P 2p, (c) and O 1s XPS spectra of CBi, GBi and GC-Bi, (d) EPR spectra, (e) and Fluorescence spectra of CBi, GBi and GC-Bi.

Among the three systems, GC-Bi demonstrated a significantly enhanced intensity of the OV peak, approximately 30% higher in integrated area compared to CBi, which reflects a higher concentration of oxygen vacancies indicating successful defect engineering.³¹ This is likely a consequence of the gelation process and amorphous domain formation, both of which facilitate lattice distortion and oxygen deficiency. Importantly, the increased OV peak intensity in GC-Bi not only confirm structural modifications but also signal a nuanced electronic reconfiguration. The

enrichment of C=O and P=O functional groups around bismuth enhances the electron withdrawing nature of the surrounding chemical environment. This, in turn, intensifies the electropositive nature of Bi³⁺ centers. To stabilize and maintain the Bi³⁺ oxidation state, bridging oxygen atoms from C-O and P-O environments (OL peak) act as electron donors, thereby increasing local electron richness, generating oxygen vacancies and consequently diminishing the intensity of the OL peak.

This enhanced electron density around Bi centers was further confirmed by the electron paramagnetic resonance (EPR) spectra, which exhibited a markedly stronger signal in GC-Bi than in the other two samples (Figure 27d). The EPR enhancement reflects the greater abundance of unpaired electrons associated with oxygen vacancies, reinforcing the conclusion that both defect sites and heterojunction interfaces contribute to the observed electronic properties.

Finally, fluorescence spectroscopy revealed a substantial quenching of emission intensity in GC-Bi compared to CBi and GBi (Figure 27e). This is a direct manifestation of suppressed electron-hole recombination, a hallmark of efficient heterojunction design and defect-mediated charge separation. Taken together, the results from XPS, EPR, and photoluminescence analyses convincingly demonstrate the successful insitu construction of a heterostructured photocatalyst with enriched oxygen vacancies and enhanced interfacial charge transfer - an ideal configuration for high-performance photocatalytic nitrogen reduction reaction (PNRR).

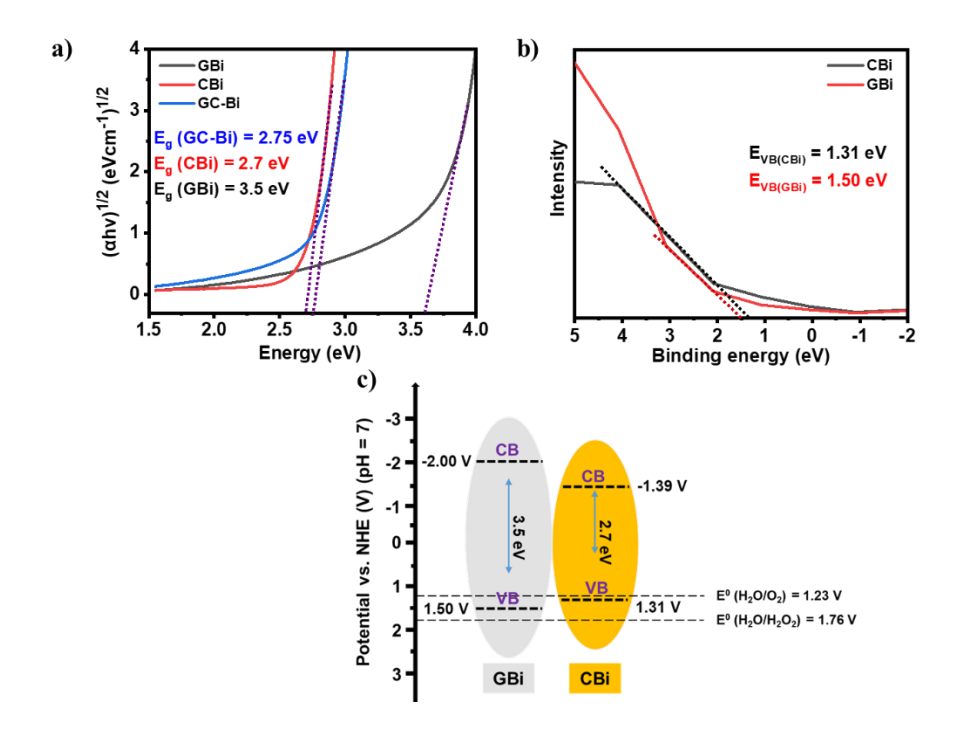


Figure 28. (a) Tauc's plot, (b) VB-XPS spectra, (c) Energy band gap structure of GC-Bi containing both CBi and GBi.

To further establish the formation of the in-situ heterojunction and understand the electronic structure of the prepared systems, a detailed band structure analysis was carried out using UV–Vis spectroscopy and valence band XPS. The optical band gaps were determined from the Tauc plots (Figure 28a), derived from the absorption spectra, revealing distinct electronic transitions in each sample. Simultaneously, valence band XPS measurements were employed to estimate the position of the valence band maxima (VBM) by extrapolating the leading edge of the spectra in the low binding energy region (Figure 28b).

By combining the optical band gap values with the VBM positions, the conduction band minima (CBM) were calculated, thereby constructing a complete picture of the energy band structure (Figure 28c). The resulting alignment clearly indicates that GC-Bi exhibits a type-I heterojunction configuration, wherein both the valence and conduction bands of CBi lie

within those of GBi. This configuration supports effective charge confinement, consistent with the suppressed fluorescence intensity and improved charge carrier separation observed earlier. The resulting energy-level structure illustrates the synergistic interaction of both components within GC-Bi, affirming the rational design of the heterostructure.

5.1.5 Plausible mechanism for photocatalytic nitrogen reduction reaction (PNRR)

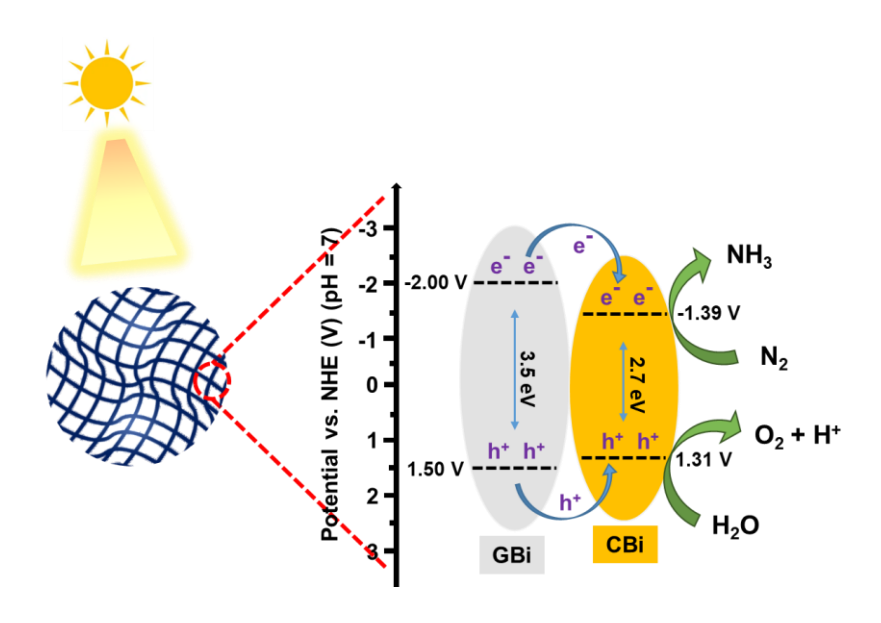


Figure 29. Plausible mechanism for photocatalytic nitrogen reduction reaction (PNRR).

The photocatalytic performance of the GC-Bi system can be rationalized by analyzing the band structure and charge carrier dynamics between its two constituents, GBi and CBi. As illustrated in Figure 29, the energy band alignment corresponds to a Type-I (straddling gap) heterojunction, wherein both the conduction band (CB) and valence band (VB) edges of GBi are located at higher energy levels compared to those of CBi. Upon irradiation with photons of energy greater than the bandgaps of both components (3.5 eV for GBi and 2.7 eV for CBi), electron-hole pairs are generated in the respective semiconductors. Due to the Type-I band alignment, photogenerated electrons in the CB of GBi spontaneously transfer to the

lower-lying CB of CBi, while the holes in the VB of GBi migrate to the VB of CBi. This results in the accumulation of both charge carriers (electrons and holes) in CBi, which serves as the primary catalytic site for subsequent redox reactions. The electrons in the CB of CBi possess sufficient reducing power to activate and reduce molecular nitrogen (N₂) to ammonia (NH₃). The standard potential for the N₂/NH₃ redox couple is approximately –1.39 V vs. NHE, and the CB position of CBi (+1.31 V vs. NHE) oxidize water molecules to generate molecular oxygen (O₂) and protons, thus maintaining charge neutrality and completing the photocatalytic cycle.

In this mechanism, GBi functions primarily as a light absorber and charge donor, whereas CBi serves as the main active site where both reduction and oxidation half-reactions take place. The spatial concentration of charge carriers within CBi minimizes recombination losses and enhances the overall efficiency of the nitrogen reduction process. The energetically favorable band positions and effective charge transfer dynamics confirm the capability of the GC–Bi system to function as a robust and recyclable photocatalyst for sustainable ammonia production under ambient conditions.

5.1.6 Mechanical Strength

Rheological testing was conducted to assess the mechanical stability and self-recovery abilities of the metalogel at 25°C. Strain, stress, and frequency sweep analyses were performed on gels with different metal ion concentrations ranging from 10 to 80 mM (Figure 30a, b). The gels with a 40 mM metal ion concentration exhibited the highest mechanical strength. The storage modulus (G') was found to be greater than the loss modulus (G''), indicating that the gels displayed more elastic than viscous properties. The yield points were observed to be at 22%, 70%, and 150% strain for GC-Bi, GBi, and GC gels, respectively. The G' and G'' values for GC-Bi and GBi were higher than those for GC, likely due to the ionic bridge effect of

the metal ion, which promotes fibril cross-linking and increases mechanical rigidity. To test the hydrogel's recoverability, a thixotropic loop test was performed, alternating between low (1%) and high (500%) strains at 100-second intervals to ensure full loss and recovery of elasticity. All gels maintained their elastic nature (G' > G'') at 1% strain but began to lose this elasticity (G'' > G') when the strain was increased to 500%. Once the strain was reduced back to 1%, the gels regained their elastic properties. The reversible sol-gel transition was observed over multiple cycles, with the gels returning to their gel state within 100 seconds, demonstrating dynamic behaviour and quick recovery of the self-assembled supramolecular network (Figure 30c-e).³²

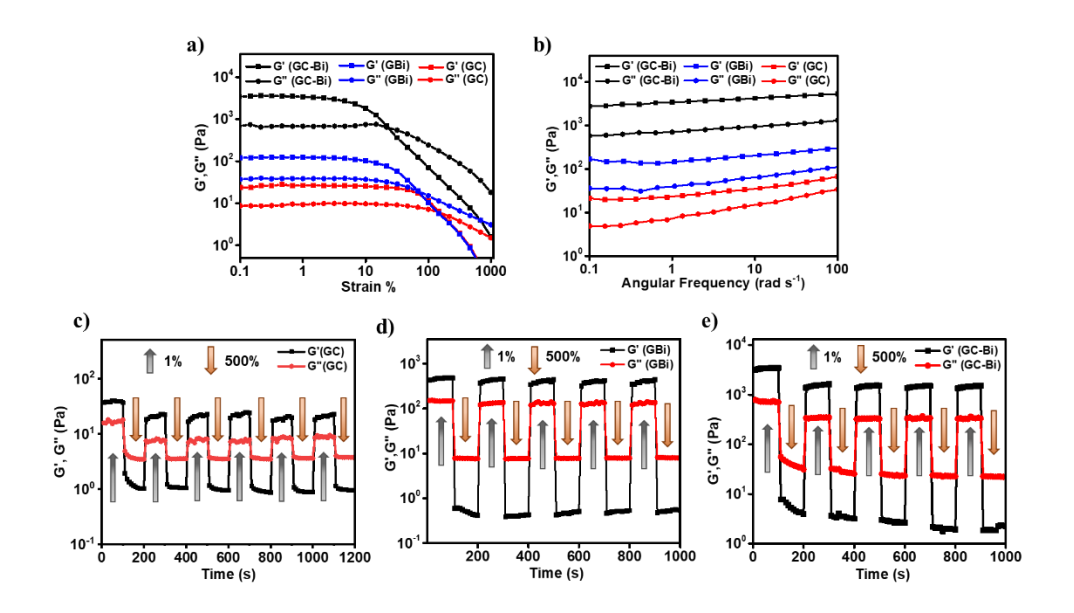


Figure 30. (a) Dynamic strain sweep of the GC, GBi, and GC-Bi gels conducted at a constant angular frequency of 10 rad/s, (b) frequency sweep tests of the GC, GBi, and GC-Bi metalogels at a constant strain of 1%, (c) thixotropic loop analysis for the GC, (d) GBi, (e) and GC-Bi metalogel.

CHAPTER 6

6.1 CONCLUSION

This research demonstrates the effective development of supramolecular hydrogels via polyphenol-directed assembly of nucleotides, overcoming the challenges associated with long-chain oligonucleotides. Using CA as a directing and cross-linking agent, GMP self-assembles to a G-quadruplex architecture, leading to the formation of a thermoreversible transparent GC hydrogel. The spectroscopic and microscopic analysis of GC hydrogel revealed the functionalization of catechol groups on the surface of Gquadruplex-driven helical fibrillar networks. The functionalization of these catechol groups opened a new avenue to exploit it as a versatile scaffold for incorporating various metal-polyphenol complexes on the G-quadruplex hydrogel system for multifunctional applications. In particular, the bismuthintegrated hydrogel (GC-Bi) exhibited exceptional photocatalytic activity, achieving a significantly enhanced ammonia yield of 905.2 µmol h⁻¹ g⁻¹ (cat.), nearly 3.8 times higher than the standalone CBi complex. Thorough investigation revealed that the in situ formation of heterojunction led to the increased oxygen vacancies and surface area, which promotes the physical and chemical adsorption of N₂ on the surface of the GC-Bi catalyst, thereby enhancing the photocatalytic N₂ fixation to NH₃. Structural and spectroscopic analyses highlighted features like mesoporosity, efficient charge separation, and stabilized electronic properties, underscoring the potential of supramolecular chemistry to bridge the structure-propertyfunction relationship and address challenges in sustainable material design.

6.2 FUTURE SCOPE

Future work will focus on expanding the scope of this strategy to include alternative polyphenols and metal ions, aiming to tune material properties for specific applications. Efforts will also be directed toward mapping active sites and elucidating reaction mechanisms to enhance catalytic efficiency. This approach offers a platform for designing scalable, recyclable materials with diverse applications, including environmental remediation, energy conversion, and carbon capture, paving the way for innovations in functional material design and sustainable technology.

CHAPTER 7

7.1 REFERENCES

- (1) Brito, J.; Hlushko, H.; Abbott, A.; Aliakseyeu, A.; Hlushko, R.; Sukhishvili, S. A. Integrating Antioxidant Functionality into Polymer Materials: Fundamentals, Strategies, and Applications. *ACS Appl. Mater. Interfaces* 2021, 13, 41372–41395. https://doi.org/10.1021/acsami.1c08061.
- (2) Xing, L.; Zhang, H.; Qi, R.; Tsao, R.; Mine, Y. Recent Advances in the Understanding of the Health Benefits and Molecular Mechanisms Associated with Green Tea Polyphenols. *J. Agric. Food Chem.* **2019**, 67, 1029–1043. https://doi.org/10.1021/acs.jafc.8b06146.
- (3) Bravo, L. Polyphenols: Chemistry, Dietary Sources, Metabolism, and Nutritional Significance. *Nutr. Rev.* **2009**, *56*, 317–333. https://doi.org/10.1111/j.1753-4887.1998.tb01670.x.
- (4) Zhou, J.; Lin, Z.; Ju, Y.; Rahim, Md. A.; Richardson, J. J.; Caruso, F. Polyphenol-Mediated Assembly for Particle Engineering. *Acc. Chem. Res.* 2020, 53, 1269–1278. https://doi.org/10.1021/acs.accounts.0c00150.
- (5) Geng, H.; Zhong, Q.-Z.; Li, J.; Lin, Z.; Cui, J.; Caruso, F.; Hao, J. Metal Ion-Directed Functional Metal—Phenolic Materials. *Chem. Rev.* **2022**, *122*, 11432–11473. https://doi.org/10.1021/acs.chemrev.1c01042.
- (6) Rahim, Md. A.; Kristufek, S. L.; Pan, S.; Richardson, J. J.; Caruso, F. Phenolic Building Blocks for the Assembly of Functional Materials. *Angew. Chem. Int. Ed.* 2019, 58, 1904–1927. https://doi.org/10.1002/anie.201807804.
- (7) Feng, Y.; Li, P.; Wei, J. Engineering Functional Mesoporous Materials from Plant Polyphenol Based Coordination Polymers. *Coord. Chem. Rev.* **2022**, *468*, 214649. https://doi.org/10.1016/j.ccr.2022.214649.

- (8) Han, Y.; Lin, Z.; Zhou, J.; Yun, G.; Guo, R.; Richardson, J. J.; Caruso, F. Polyphenol-Mediated Assembly of Proteins for Engineering Functional Materials. *Angew. Chem. Int. Ed.* 2020, 59, 15618–15625. https://doi.org/10.1002/anie.202002089.
- (9) Qu, Y.; De Rose, R.; Kim, C.-J.; Zhou, J.; Lin, Z.; Ju, Y.; Bhangu, S. K.; Cortez-Jugo, C.; Cavalieri, F.; Caruso, F. Supramolecular Polyphenol-DNA Microparticles for In Vivo Adjuvant and Antigen Co-Delivery and Immune Stimulation. *Angew. Chem. Int. Ed.* 2023, 62, e202214935. https://doi.org/10.1002/anie.202214935.
- (10) Qu, Y.; Zhu, H.; Lin, Z.; Vanni, D.; Bhangu, S. K.; Dyett, B.; Sani, M.-A.; Cortez-Jugo, C.; Caruso, F.; Cavalieri, F. Supramolecular Assembly of Polyphenols and Nucleic Acids by Thermal Cycling for Immune Cell Activation. *Chem. Mater.* **2023**, *35*, 7103–7112. https://doi.org/10.1021/acs.chemmater.3c01378.
- (11) Sikder, A.; Esen, C.; O'Reilly, R. K. Nucleobase-Interaction-Directed Biomimetic Supramolecular Self-Assembly. *Acc. Chem. Res.* **2022**, *55*, 1609–1619. https://doi.org/10.1021/acs.accounts.2c00135.
- (12) Davis, J. T. G-Quartets 40 Years Later: From 5'-GMP to Molecular Biology and Supramolecular Chemistry. *Angew. Chem. Int. Ed.* **2004**, 43, 668–698. https://doi.org/10.1002/anie.200300589.
- (13) Davis, J. T.; Spada, G. P. Supramolecular Architectures Generated by Self-Assembly of Guanosine Derivatives. *Chem. Soc. Rev.* **2007**, *36*, 296–313. https://doi.org/10.1039/B600282J.
- (14) Ma, T.; Li, R.; Huang, Y.-C.; Lu, Y.; Guo, L.; Niu, M.; Huang, X.; Soomro, R. A.; Ren, J.; Wang, Q.; Xu, B.; Yang, C.; Fu, F.; Wang, D. Interfacial Chemical-Bonded MoS₂/In–Bi₂MoO₆ Heterostructure for Enhanced Photocatalytic Nitrogen-to-Ammonia Conversion. *ACS Catal.* **2024**, *14*, 6292–6304. https://doi.org/10.1021/acscatal.3c05416.
- (15) Chakraborty, A.; Rani, A.; Sinha, P.; Sarma, S.; Agarwal, V.; Prasun, A.; Jha, H. C.; Sarma, T. K. Guanosine Monophosphate Induced Solubilization of Folic Acid Leading to Hydrogel Formation for

- Targeted Delivery of Hydrophilic and Hydrophobic Drugs. *ACS Appl. Mater. Interfaces* **2025**, *17*, 11848–11860. https://doi.org/10.1021/acsami.4c21306.
- (16) Sarma, S.; Thakur, N.; Varshney, N.; Jha, H. C.; Sarma, T. K. Chromatin Inspired Bio-Condensation between Biomass DNA and Guanosine Monophosphate Produces All-Nucleic Hydrogel as a Hydrotropic Drug Carrier. *Commun. Chem.* **2024**, *7*, 1–13. https://doi.org/10.1038/s42004-024-01353-6.
- (17) Chakraborty, A.; Dash, S.; Thakur, N.; Agarwal, V.; Nayak, D.; Sarma, T. K. Polyoxometalate-Guanosine Monophosphate Hydrogels with Haloperoxidase-like Activity for Antibacterial Performance. *Biomacromolecules* 2024, 25, 104–118. https://doi.org/10.1021/acs.biomac.3c00845.
- (18) Thakur, N.; Sharma, B.; Bishnoi, S.; Jain, S.; Nayak, D.; Sarma, T. K. Biocompatible Fe³⁺ and Ca²⁺ Dual Cross-Linked G-Quadruplex Hydrogels as Effective Drug Delivery System for pH-Responsive Sustained Zero-Order Release of Doxorubicin. *ACS Appl. Bio Mater.* **2019**, 2, 3300–3311. https://doi.org/10.1021/acsabm.9b00334.
- (19) Li, X.; Sánchez-Ferrer, A.; Bagnani, M.; Adamcik, J.; Azzari, P.; Hao, J.; Song, A.; Liu, H.; Mezzenga, R. Metal Ions Confinement Defines the Architecture of G-Quartet, G-Quadruplex Fibrils and Their Assembly into Nematic Tactoids. *Proc. Natl. Acad. Sci.* **2020**, *117*, 9832–9839. https://doi.org/10.1073/pnas.1919777117.
- (20) Zhou, J.; Lin, Z.; Penna, M.; Pan, S.; Ju, Y.; Li, S.; Han, Y.; Chen, J.; Lin, G.; Richardson, J. J.; Yarovsky, I.; Caruso, F. Particle Engineering Enabled by Polyphenol-Mediated Supramolecular Networks. *Nat. Commun.* **2020**, *11*, 4804. https://doi.org/10.1038/s41467-020-18589-0.
- (21) Ejima, H.; Richardson, J. J.; Liang, K.; Best, J. P.; van Koeverden, M. P.; Such, G. K.; Cui, J.; Caruso, F. One-Step Assembly of Coordination

- Complexes for Versatile Film and Particle Engineering. *Science* **2013**, *341*, 154–157. https://doi.org/10.1126/science.1237265.
- (22) Xia, P.; Song, Y.-J.; Liu, Y.-Z.; Long, M.-X.; Yang, C.; Zhang, X.-Y.; Zhang, T. Advances in the Optical and Electronic Properties and Applications of Bismuth-Based Semiconductor Materials. *J. Mater. Chem. C* **2024**, *12*, 1609–1624. https://doi.org/10.1039/D3TC03329E.
- (23) Shi, M.; Yang, H.; Zhao, Z.; Ren, G.; Meng, X. Bismuth-Based Semiconductors Applied in Photocatalytic Reduction Processes: Fundamentals, Advances and Future Perspectives. *Chem. Commun.* **2023**, *59*, 4274–4287. https://doi.org/10.1039/D3CC00580A.
- (24) Sahu, T. K.; Gupta, A.; Agarwal, V.; Sarma, T. K. Facile Synthesis of Enzyme-Mimicking Cobalt-Polyphenol Coordination Network for Oxidation of Phenolic Pollutants. *ACS Appl. Eng. Mater.* **2023**, *1*, 3194–3204. https://doi.org/10.1021/acsaenm.3c00487.
- (25) Liu, S.; Ren, G.; Meng, X. BrO₃⁻ Bridge Bi₂O₃/Bi(OH)₃ Heterojunction with Multiple Charge Transfer Channels for Efficient Photocatalytic Nitrogen Fixation and CO2 Reduction. *ACS Sustain. Chem. Eng.* **2023**, *11*, 15599–15608. https://doi.org/10.1021/acssuschemeng.3c04137.
- (26) Hao, Y.-C.; Guo, Y.; Chen, L.-W.; Shu, M.; Wang, X.-Y.; Bu, T.-A.; Gao, W.-Y.; Zhang, N.; Su, X.; Feng, X.; Zhou, J.-W.; Wang, B.; Hu, C.-W.; Yin, A.-X.; Si, R.; Zhang, Y.-W.; Yan, C.-H. Promoting Nitrogen Electroreduction to Ammonia with Bismuth Nanocrystals and Potassium Cations in Water. *Nat. Catal.* **2019**, *2*, 448–456. https://doi.org/10.1038/s41929-019-0241-7.
- (27) Li, P.; Gao, S.; Liu, Q.; Ding, P.; Wu, Y.; Wang, C.; Yu, S.; Liu, W.; Wang, Q.; Chen, S. Recent Progress of the Design and Engineering of Bismuth Oxyhalides for Photocatalytic Nitrogen Fixation. *Adv. Energy Sustain. Res.* **2021**, 2, 2000097. https://doi.org/10.1002/aesr.202000097.

- (28) Huang, X.; Du, R.; Ren, J.; Li, X.; Fu, M.; Fu, S.; Ma, T.; Guo, L.; Soomro, R. A.; Yang, C.; Wang, D. Unveiling the Mechanism of Aerobic Photocatalytic Nitrogen Fixation over Dynamic Structural Renovation on Bi₂MO₆ (M = Mo, W). *ACS Catal.* **2024**, *14*, 13542–13549. https://doi.org/10.1021/acscatal.4c03183.
- (29) Lee, J.; Tan, L.-L.; Chai, S.-P. Heterojunction Photocatalysts for Artificial Nitrogen Fixation: Fundamentals, Latest Advances and Future Perspectives. *Nanoscale* **2021**, *13*, 7011–7033. https://doi.org/10.1039/D1NR00783A.
- (30) Zhang, Y.; Zhang, J.; Yi, Q.; Wang, F.; Fu, H.; Gao, H.; Liao, Y. In Situ Construction of Porous β-Bi₂O₃/BiOCOOH Heterojunction Photocatalysts: Enhancing Nitrogen Fixation Activity by the Synergistic Effect of Oxygen Vacancies and Lattice Oxygen. ACS Appl. Energy Mater. 2022, 5, 9503–9511. https://doi.org/10.1021/acsaem.2c01136.
- (31) A. Mohamed, W.; Chakraborty, J.; Bourda, L.; Lavendomme, R.; Liu, C.; Morent, R.; De Geyter, N.; Van Hecke, K.; Kaczmarek, A. M.; Van Der Voort, P. Engineering Porosity and Functionality in a Robust Twofold Interpenetrated Bismuth-Based MOF: Toward a Porous, Stable, and Photoactive Material. *J. Am. Chem. Soc.* **2024**, *146*, 13113–13125. https://doi.org/10.1021/jacs.3c14739.
- (32) Chakraborty, A.; Ghosh, T.; Sarma, S.; Agarwal, V.; Kumar, R.; K Sarma, T. A Multi-Stimuli Responsive Polyoxometalate-Guanosine Monophosphate Hybrid Chromogenic Smart Hydrogel. *J. Mater. Chem. C* 2024, 12, 13447–13456. https://doi.org/10.1039/D4TC01973C.

7.2 SUPPORTING FIGURES

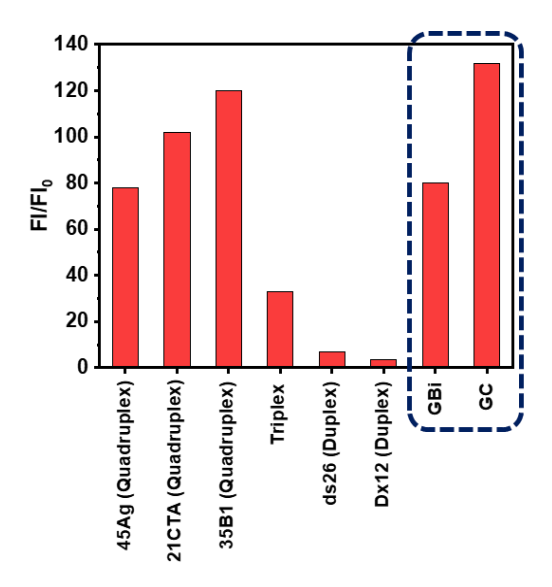


Figure S1. Comparison of ThT fluorescence increase in the previous reported systems of G-assemblies with Gbi and GC.

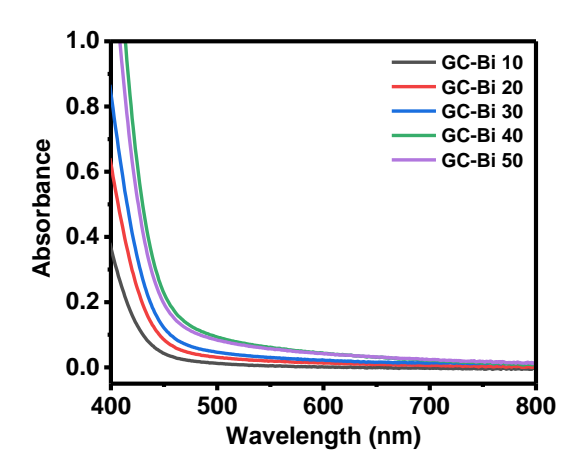


Figure S2. UV-Vis absorbance spectra of GC-Bi gel with varying Bi³⁺ conc. (10–50 mM)

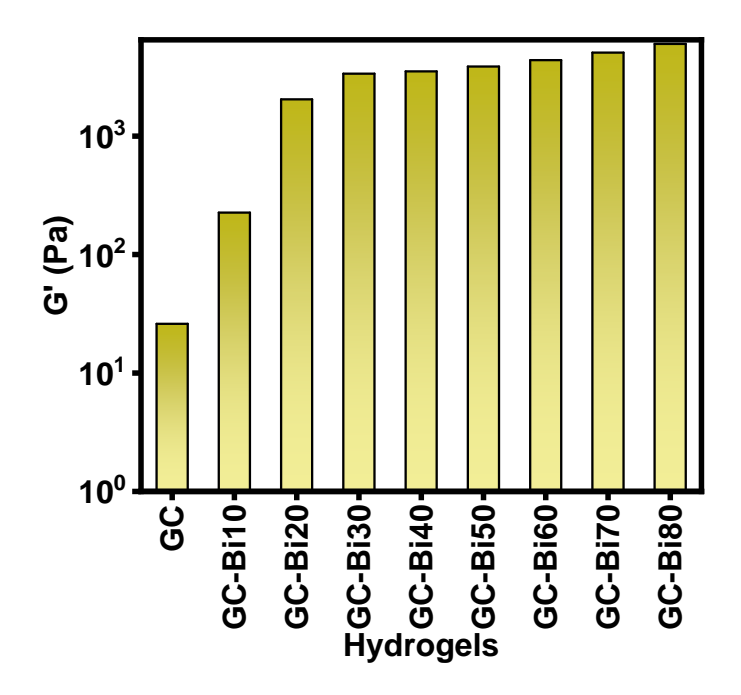


Figure S3. Concentration-dependent rheological experiment GC-Bi hydrogels by varying Bi³⁺ conc. from 10 mM to 80 mM.

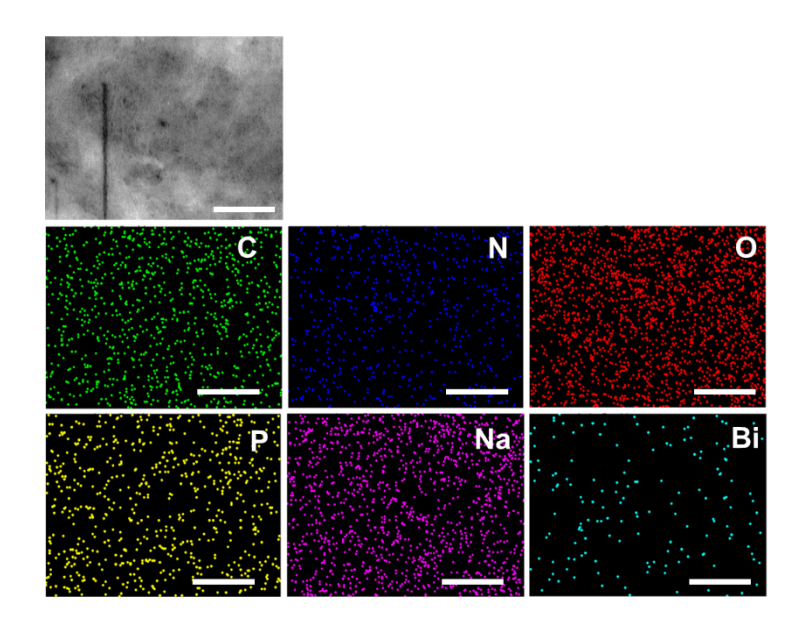


Figure S4. EDX elemental mapping (C, N, O, P, Na, Bi) of GC-Bi gel.

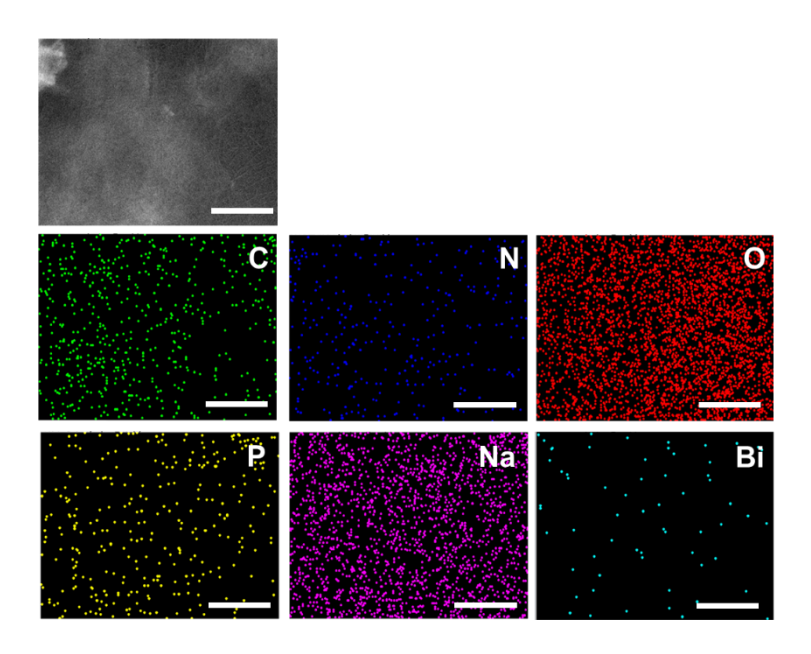


Figure S5. EDX (C, N, O, P, Na, Bi) of GBi gel.

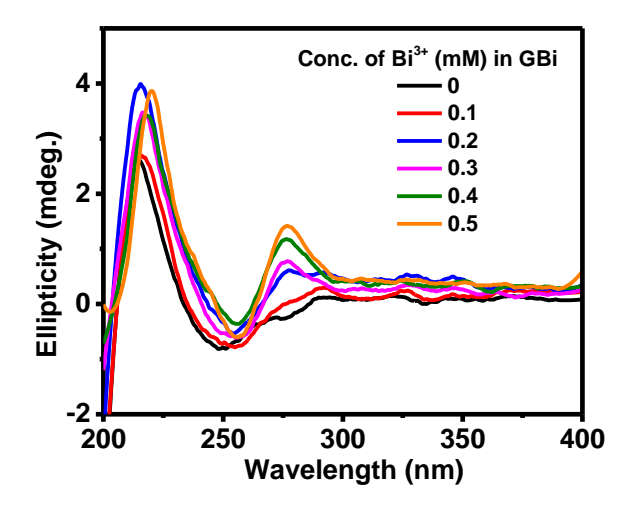


Figure S6. CD spectra of GBi gel with varying Bi³⁺ conc. (0–50 mM).

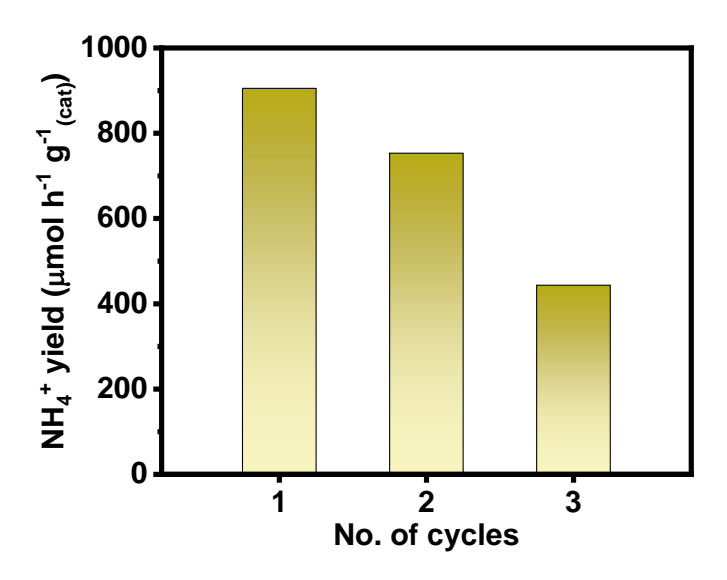


Figure S7. Recyclability of PNRR using GC-Bi as catalyst.

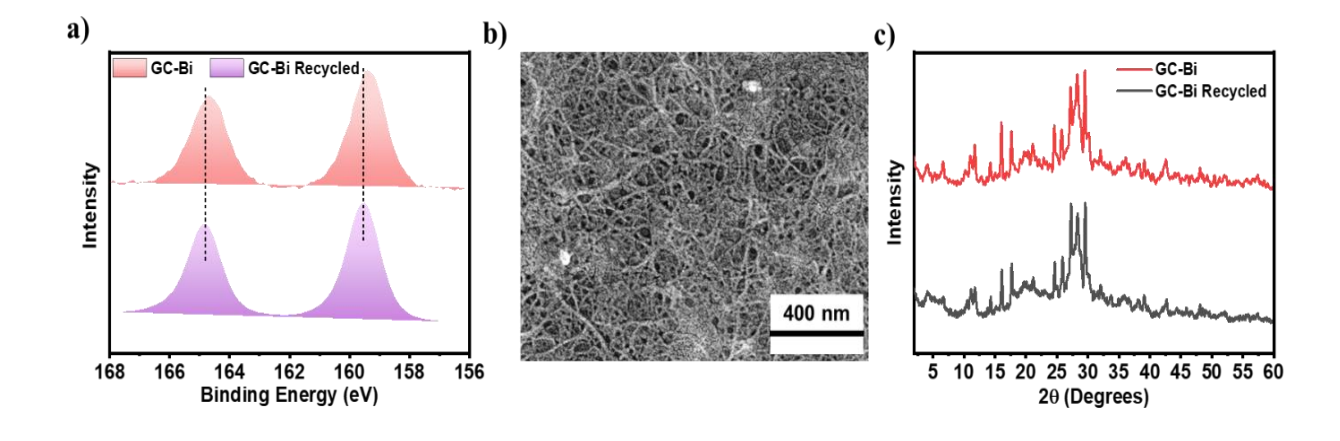


Figure S8. (a) Bi 4f XPS spectra, (b) SEM image, (c) and PXRD spectra of recycled GC-Bi.

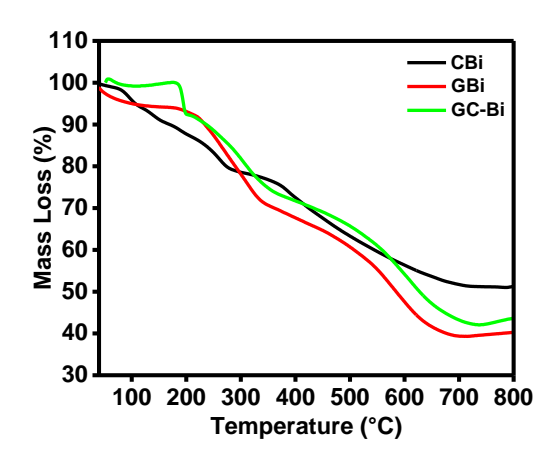


Figure S9. Thermogravimetric analysis of CBi, GBi and GC-Bi.

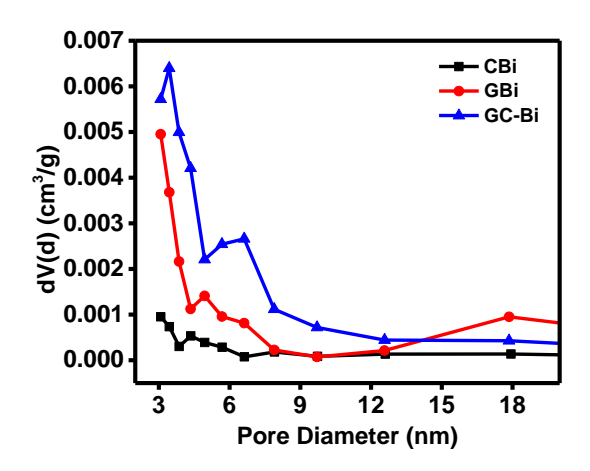


Figure S10. Pore size and pore volume analysis of CBi, GBi and GC-Bi.

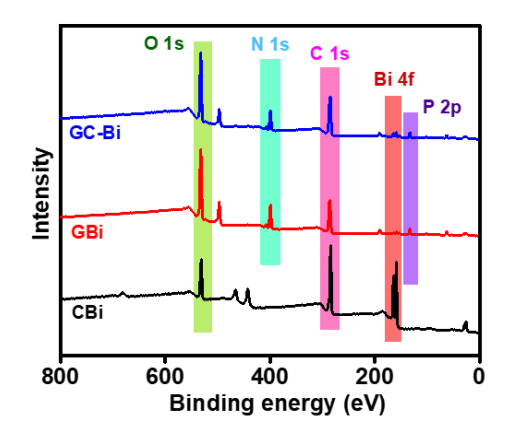


Figure S11. XPS survey spectra of CBi, GBi and GC-Bi